ENHANCED EARLY DETECTION OF ORAL SQUAMOUS CELL CARCINOMA VIA STRUCTURED ILLUMINATION FLUORESCENCE LIFETIME IMAGING

A Dissertation

by

TAYLOR A. HINSDALE

Submitted to the Office of Graduate and Professional Studies of
Texas A&M University
in partial fulfillment of the requirements for the degree of

DOCTOR OF PHILOSOPHY

Chair of Committee,	Kristen C. Maitland
Committee Members,	Javier A. Jo
	Alvin T. Yeh
	Mark Lenox
Head of Department,	Mike McShane

May 2018

Major Subject: Biomedical Engineering

ABSTRACT

The early diagnosis of oral carcinoma has proven to be a difficult task. Fully developed oral squamous cell carcinomas can be easily recognized by trained clinicians due to the appearance of aggressive exogenous tumors and other visual and textural changes. However, pre-malignancies that can lead to oral squamous cell carcinoma are often difficult to diagnose due to their similar appearance to normal or benign oral tissue. The gold standard for diagnosis continues to be visual and palpatory inspection by a clinician which may be followed by an exploratory biopsy on suspicious lesions. This excised lesion is then sent for histopathological analysis and a recommendation is made based on the results. One of the flaws with this methodology is that the clinical diagnosis of oral carcinomas and pre-malignancies is subjective, and opinions can vary between clinicians. Additionally, achieving a histopathological diagnosis of a tissue sample and acting on that information takes a significant amount of time. Automation of the clinical diagnosis of oral cancers by utilizing optical imaging and image recognition techniques could drastically reduce this time.

Two promising modalities for cancer imaging are structured illumination and fluorescence lifetime imaging microscopy. Oral epithelial tissue undergoing carcinogenesis is subject to biochemical changes caused by fundamental shifts in the epithelial metabolism. This shift in the metabolism and biochemical state causes a change in the cellular microenvironment that can affect how long certain endogenous fluorophores emit light. This phenomenon can be probed by fluorescence lifetime

imaging. Although fluorescence lifetime imaging offers an exceptional ability to distinguish between different fluorophores within the focal plane of an imaging system, it suffers from the inability to accurately resolve multiple spectrally overlapping lifetimes that exist within a single pixel. The fluorophores of interest in oral carcinoma, NADH and FAD, share significant spectral overlap with collagen, an endogenous fluorophore in the submucosal connective tissue. Because collagen generally overlaps laterally with NADH and FAD, its fluorescence emission is usually found in both the NADH and, to a lesser extent, FAD channels. Luckily, the collagen containing connective tissue is exclusively deep relative to the oral epithelium. This axial spatial separation allows for the utilization of optical sectioning to spatially isolate NADH and FAD from the effects of collagen rather than spectrally. This thesis presents the development and testing of a fluorescence lifetime imaging microscope with optical sectioning capability provided by structured illumination with the goal of enhancing the early detection of oral carcinoma.

ACKNOWLEDGEMENTS

I would like to use this section to thank all of the people who have supported me throughout my education. First, I would like to thank Dr. Kristen C. Maitland for her guidance during my Ph.D. education. She was always very open and supportive of any questions that I had, whether they were regarding research, writing, or general advice. I would also like to thank Dr. Bilal H. Malik whose grant project I worked on. Collaborating with him has been a pleasure and allowed me to refine my research skills. My other committee members: Dr. Javier A. Jo, Dr. Alvin T. Yeh, and Dr. Mark Lenox, have also been a great support to my work and were always willing to sit down and discuss my research. For this, I am appreciative and extend my gratitude. Dr. Maryellen L. Giger has also been a wonderful advisor who has been a pleasure to collaborate with.

My family has also been indispensable on my journey to a Ph.D. My mother, Wendy, father, Andy, and sister, Shannon, have been continuing sources of support that have encouraged me to pursue my interests to the fullest extent. Without them, I would not have had the freedom to do what I have done and end up where I am today. I would also like to acknowledge my colleagues, Madeleine Durkee and Cory Olsovsky, who I have had to opportunity to work with during my Ph.D. They were always supportive and a tremendous help to me. I would also like to thank the rest of my friends and family who have been an immeasurable source of support during my education.

CONTRIBUTORS AND FUNDING SOURCES

Contributors

The work in this thesis was supported by Dr. Kristen C. Maitland, Dr. Javier A. Jo, and Dr. Alvin T. Yeh, from the Biomedical Engineering Department of Texas A&M University, and Dr. Bilal H. Malik and Dr. Mark Lenox of QT Ultrasound. All contributors are members of the thesis committee for this work.

Funding

Funding for this thesis was provided in part by the Texas A&M University Institute for Advanced Study HEEP Fellowship. Funding was also provided by the following grants: NIH R01CA138653, NSF CBET-1254767, NIH R03 CA191860, and NPRP 8-1606-3-322.

TABLE OF CONTENTS

Page

LIST OF FIGURES

Page

LIST OF TABLES

Page

CHAPTER I

INTRODUCTION

1.1 Prelude

Cancer is one of the most pervasive and commonly known diseases to exist in our modern world. The majority of the work in this dissertation is directed towards the enhanced early detection of oral cancer with the goal of increasing survivability rates through the early detection of oral squamous cell carcinomas. This dissertation will cover a basic overview of cancer biology, the epidemiology of cancer in the United States of America (US) and the world, oral cancer and its specific problems, current diagnostic techniques, and the development and characterization of imaging methods to enhance early detection.

1.2 Cancer biology background and overview

Cancer is a disease that is characterized by the effective misregulation of the cellular reproductive processes.[1] The current understanding of cancer states that it is a multi-gene, multi-stage disease that originates from a single abnormal cell.[1] Through several iterations of successive division, this single abnormal cell eventually forms a tumor mass. This process repeats and results in the expansion and growth of the tumor tissue. Cancer becomes a mortal danger when these cells, with unregulated reproductive patterns, begin to spread and disrupt the homeostasis of the tissue that they are in. This can become even more of a problem if the tumor cells enter the blood stream and circulate to other parts of the body in a process known as metastasis.[2] These metastatic

cells have the potential to create tumors over many regions and cause serious bodily dysfunction.

Cancer is considered to be caused by a combination of two factors, genetics and environment. Evidence shows that environment plays a critical role in determining the probability of developing cancer. For example, alcohol and tobacco use increase the risk of developing several types of cancer.[3] There are several other cases showing the environmental factors to be catalysts for cancer development. Incidence of stomach cancer is 6-8 times higher in Japanese populations when compared to Americans, but the incidence of stomach cancer in the children of Japanese immigrants is relatively equal to that of their American peers.[1] This suggests that environmental factors in Japan had a significant effect on the population's cancer risk. Smoking has been extensively studied as an environmental impact factor and shown to increase the risk of developing certain types of cancer.[4] These facts suggest that, while cancer may not be able to be completely eradicated, due to its genetic component, education about the risk factors and better preventative healthcare could have a large impact on cancer incidence and mortality.

1.3 Cancer as a disease in the United States of America and the world

Cancer is a nationwide health problem in the US, taking a toll on its people's health and being a burden on the nation's healthcare systems. In 2016, an estimated 1,685,210 new cases of cancer were diagnosed, engendering 595,690 deaths.[5] Nearly 1 in 200 men and women are newly diagnosed each year with some form of cancer. Among the most common are: breast cancer, lung and bronchus cancer, prostate cancer,

colon and rectum cancer, bladder cancer, melanoma of the skin, non-Hodgkin lymphoma, thyroid cancer, kidney and renal pelvis cancer, leukemia, endometrial cancer, and pancreatic cancer. In addition to being a prevalent disease, over one third of cancer diagnoses result in patient mortality. However, perhaps due to increased awareness and better diagnostic techniques, cancer occurrence rates are stabilizing in the US. The current state of affairs for cancer is that the overall age-adjusted mortality and incidence rates have declined for men, while the incidence rate for women is stable and the mortality rate is on the decline.[6] These trends were evaluated from data comparing men and women from all major ethnic and racial groups. Although the cancer rates in the US are on the decline or stabilizing, it is still one of the leading causes of death in the Unites States of America, second only to heart disease.[7]

Although cancer rates in the US as a whole appear to be stabilizing, this is far from the case throughout the entire world. According to the World Health Organization (WHO) estimates for 2011, cancer will be one of the leading causes of death in low and middle income countries over the next decades, outpacing both coronary heart disease and stroke incidence.[8] To put the global health aspect of cancer into perspective, nearly 1 in 6 deaths today are caused by cancer with 70% of these cancer related deaths coming from low and middle-income countries.[9] There is clearly a difference in the trends and statistics when comparing the populations of the US against the world as a whole.

1.4 Oral squamous cell carcinoma

Oral squamous cell carcinoma (OSCC) is a cancer that is commonly characterized by a poor prognosis and a low survival rate.[10] Oral cancer is of particular interest because incidence rates have been on the rise, increasing by 0.6% per year between 2004-2014.[11] This increase in incidence suggests that oral cancer is dependent on environmental factors and population behaviors. The sudden rise in incidence rate has been extensively studied and a consensus has been reached on some of the most dangerous risk factors. Alcohol and chewing or smoking tobacco, especially when combined, are the main risk factors associated with OSCC, but viruses, such as the human papilloma virus (HPV), and genetic predisposition also present real risk factors.[10, 12] Additionally, it has been reported that diets low in fruits and vegetables contribute to an increased risk of developing oral cancer.[13]

Oral cancer is not just a problem in the US, but is a prevalent disease worldwide. Many countries have even higher incidence rates than the US. Mortality rates are also not necessarily directly correlated with the wealth of a country, with France having a low incidence rate but a high mortality rate and Canada possessing the opposite.[14] However, many Southeast Asian countries have medium to high incidence and mortality rates. Many countries are seeing the same trends in oral cancer with increasing incidence.

If oral cancer metastasizes, patients are much more likely to die, but even those who survive treatment often have a drastically reduced quality of life.[15] Treatment often involves destructive facial surgery to remove the cancerous tissue which can

drastically alter the physical appearance of the individual. These changes may have many effects including: appearance and function (eating, drinking, swallowing and speaking), nutritional deficiencies resulting from poor function, as well as mental health issues.[15] The high chance for morbidity with oral cancer, when compared to other cancers, provides an extra incentive to diagnosis cancerous tissue as early as possible.

1.5 Current methods of diagnosis

Current practice dictates that patients be routinely screened for signs of certain types of cancer, even if they show no outward symptoms. The accepted definition of screening is as follows: “the application of a test or tests to people who are apparently free from the disease in question in order to sort out those who probably have the disease from those who probably do not”.[16, 17] Screening should then follow as a relatively common place procedure that is given to the majority of the population with regular access to medical care. One of the most important provisions from the Affordable Care Act (ACA) states that private insurers shall, at the very least, provide coverage for and not impose any cost sharing measures on preventative medicine procedures.[18] This helped ensure that proper screening measures could be implemented with the entire US population without patients incurring medical debt. A few well established screening procedures have been shown to greatly reduce patient morbidity and mortality.[16] Some of the most common screening procedures that one might recognize are Pap smears to look for cervical cancer and mammograms to screen for breast cancer.[16] Other cancers with well-established screening procedures are colorectal cancer, prostate

cancer, skin cancer, lung cancer (for those with a history of smoking), and ovarian cancer.[19]

The standard clinical practice for detecting OSCC is by conventional oral examination where a clinician will identify areas of interest for biopsy, either visually or by palpation, and take one or more biopsies for histopathological analysis.[16] After the visual or tactile identification of a suspicious legion, a biopsy is taken and sent out for histopathological analysis. The pathologist will then fix and slice the tissue biopsy into thin 5-10 µm sections so that individual nuclear planes can be evaluated under a widefield light microscope. These slices are evaluated for the morphology and arrangement of the nuclei and their surrounding tissue.[20] A diagnosis with the current tissue pathology is given, which a clinician can use to decide what further actions need to be taken. Although this technique can be effective, it is relatively subjective, slow, and relies heavily on experienced clinicians to provide an accurate diagnosis of the biopsy.

Brush cytology is a potential candidate for use as a screening method for oral cancer, but significant oversights were made in the original clinical studies.[16] Class II lesions—lesions that would not normally be biopsied—were evaluated with brush cytology but not by scalpel biopsy. No concrete conclusion can be drawn about the method's true sensitivity and specificity without this information. Another possible oral cancer screening method is toluidine blue staining. Toluidine has been shown to be a potentially useful tool for diagnosing possible malignancies. However, even though

there is a large amount of data regarding the dye as a cancer screening tool, a lack of proper testing procedures has limited the usefulness of the data.[16]

A more attractive option than the previous examples would be to provide an optical method for identifying pre-cancerous and cancerous lesions that can use classification algorithms to isolate the tissue of interest and draw accurate margins for excision or to replace exploratory biopsies altogether. The main benefit of using an optical system that can instantly detect the pathology of the tissue is that the turnover rate for patient care can be increased. Currently there are many forms of oral optical imaging for precancerous and cancerous lesion detection such as reflectance confocal microscopy (RCM), widefield fluorescence microscopy, narrow band imaging, fluorescence lifetime imaging microscopy (FLIM), and many others.[21-25] All of these methods attempt to measure quantifiable and unique features that change between normal and precancerous tissue, and all of them possess their own unique challenges. For example, confocal microscopy has the potential to be used as a replacement for physical biopsy. Confocal is attractive because, unlike widefield imaging techniques, it preserves spatial distribution information in thick samples by utilizing optical sectioning. This is achieved by raster scanning a focused point of light across a sample with collection provided by a physical pinhole. The pinhole only accepts light from the imaging plane while blocking light from out of focus planes. This technique is useful for evaluating tissue morphology and nuclear distribution within the epithelium. However, confocal microscopy suffers from a tradeoff between field of view and imaging speed for a given resolution. Because the beam is raster scanned, collecting the image pixels in

series, it is inherently slower for a given field of view (FOV) and numerical aperture than parallel imaging techniques, such as imaging with a CCD camera. As of the writing of this dissertation, there is yet to be an effective optical *in vivo* clinical screening method, to the best of our knowledge.

1.6 Proposed method - fluorescence lifetime imaging microscopy coupled with structured illumination microscopy

FLIM is an imaging modality that can be used to analyze precancerous epithelial tissue. FLIM uses the concept of fluorescence lifetime to achieve a spatial map of chemical or biochemical content. Every fluorophore has a lifetime that is characteristic of that fluorophore. This means that when the fluorophore is stimulated by an excitation photon, the emission photon takes a characteristic amount of time to be emitted. This process can be affected by the changes in the fluorophore's environment, such as the fluorophore binding to another molecule. Nicotinamide adenine dinucleotide (NADH) and flavin adenine dinucleotide (FAD) are important markers in cellular metabolism and are also endogenous fluorophores. Precancerous tissues show a change in cellular metabolism which alters the molecular environment of NADH and FAD, altering their intrinsic lifetime. NADH and FAD's emissions are separated spectrally, but there are other fluorescent markers in the epithelium, specifically collagen, that spectrally overlap with NADH and FAD. Collagen can alter the perceived lifetimes of NADH and FAD because it lacks lateral separation in addition to spectral separation. This causes its fluorescence to be imaged in the same pixels as NADH and FAD. However, because collagen is located in the submucosa, below the NADH and FAD containing epithelium,

it is axially separated from our metabolic cofactors. This work aims to create optically sectioned lifetime images of the epithelium by using the widefield imaging technique of structured illumination microscopy (SIM) to reduce the effects of collagen fluorescence.

1.7 Fluorescence lifetime imaging microscopy

1.7.1 Fluorescence

Fluorescence is the phenomenon of matter absorbing light of a given wavelength and subsequently emitting light at another, lower energy, wavelength. Here, light is defined as an electromagnetic wave that spans a large spectrum of frequencies. We most commonly associate the word light with electromagnetic waves in the visible spectrum that ranges in wavelength from 400-700 nm, however there is also a broad range of wavelengths not directly visible to the human eye. Light can be thought of in two fundamental but different ways; it can be described as a wave or as being comprised of individual discrete units known as photons. This wave-particle duality is discussed in quantum mechanics. It can even be shown that electrons and protons have their own associated wavelengths, although it is not as trivial as discerning the wavelength of light.

Our understanding of light interaction on an atomic scale comes from quantum mechanics. As the name suggests, quantum mechanics explores the theory that interactions on a very small scale can become quantized in their behavior given the right circumstances. To help explain quantization, we can relate back to the way we observe our daily lives by considering the energy a rock gains when it is lifted off the ground. In the macroscopic world, gravitational potential energy, relative to earth, is a continuous equation that is defined by the mass of an object and the height from which it is raised

from the ground. This continuity principle is true for Newtonian mechanics, or classical mechanics, in general. If gravitational potential energy were quantized, only certain discrete energies would be allowed. What this means is that instead of the being able to smoothly lift a rock off of the ground and have its gravitational potential energy smoothly rise with it, the rock would jump from the ground up to the next energy level, or height, with sufficient “lifting” applied. Again, with more “lifting”, it would jump again. Admittedly, this would appear quite odd and unsettling to an observer. Because these quantization effects generally only occur on an atomic scale, we do not observe this in everyday life.

One of the most fundamental examples used to illustrate quantum mechanics is a single electron trapped inside a potential well, commonly known as the “quantum box” thought experiment.[26] Suppose an electron in a two dimensional plane is trapped between two infinite potential energies. Because the electron doesn’t have enough energy to exceed the confining potential and escape, it remains within the well. However, it is possible for this electron to exist in several discrete energy states within the well, which can be derived from Schrödinger’s equation. The electron will most likely remain in its lowest energy state, the ground state, unless acted on by an outside factor. This scenario is analogous to electrons orbiting an atom. In fluorescence, as mentioned earlier, the electron in this scenario would absorb an incoming photon, the outside factor, and be promoted to a higher energy level. It would then fall back down to its ground state and stabilize. The return to the ground state releases a photon and is the

phenomenon known as fluorescence. It should be noted that fluorescence is not entirely explained by Schrödinger's equation and further inquiry into the subject is required.

Spontaneous emission describes the process of excited electrons spontaneously transferring from their excited energy levels back down to their ground state and emitting a photon. In order to properly explain this, the theory of quantum electrodynamics (QED) is required. In particular, this theory focuses on the quantization of the electromagnetic field and its interaction with matter. Essentially, QED states that an atom and its electronic state interact with the electromagnetic (EM) field, and the EM field's quantized state, as a system.[27-30] The quantized electromagnetic field has a vacuum-energy, or zero point energy, that allows for the spontaneous transitions between excited electronic states to their ground states to occur. A proposed mechanism is that the fluctuations in the vacuum-energy of the EM field can perturb the excited electron by interacting with its dipole moment and cause a transition. However, there is still some debate regarding this topic. The rate at which this spontaneous emission occurs can also be conveyed in terms of the thermodynamic state of the system as described by Einstein.[31]

The fluorescence lifetime of a molecule is directly related to the spontaneous decay rate just described. This spontaneous decay rate, more accurately described as the probability of decay, is designated as Einstein's *A* coefficient and can be derived from Einstein's thermodynamic treatment of a two-level system. For example, consider the following derivation in Equation 1 [32].

Equation 1

$$N(t) = number\ of\ emitters\ in\ excited\ state$$

$$\frac{dN(t)}{dt} = A * N(t)$$

$$N(t) = N(0)e^{(t/\tau)}, where\ \tau = 1/A$$

$N(t)$ is defined as the number of emitters in an excited state, i.e. the number of molecules that have absorbed a photon and have been promoted to an excited electronic state. A is Einstein's spontaneous decay coefficient. τ is what is commonly referred to as the lifetime of the excited state. One thing to note is that this derivation did not account for the influence of non-radiative decay processes on lifetime. Equation 1 gives the essential mathematical distribution of photons emitted over time via spontaneous emission during fluorescence. To summarize, if a fluorophore is stimulated by an impulse of light, a population of electrons will be excited to a higher energy level. This population of electrons will then transition back down to the ground state and emit an ensemble of photons due to spontaneous emission. These photons, which are emitted over a duration of time, follow the negative exponential distribution described in Equation 1.

FLIM has garnered popularity as a valuable tool for analyzing biological samples. Perhaps one of its most important qualities is that the measurement of fluorescence lifetime is largely independent of fluorescence intensity, excitation intensity, and detection efficiency.[33] These unique measurement properties remove much of the variability normally associated with biological samples and allows for the extraction of a quantitative parameter, fluorescence lifetime. Some examples of uses for

FLIM include, but are not limited to: ion imaging, oxygen imaging, and local microenvironment sensing.[33, 34] Ion imaging can be used to measure changes in the amount of calcium present within a sample because certain fluorescent dyes will change their lifetime in the presence of calcium. This process usually occurs due to the reduction in the quantum yield of the dyes when they bind with calcium. Because calcium is one the most important neurotransmitters in the body, FLIM can be used to monitor various aspects of neural function.[35]

In our case, the most important use for FLIM is its ability to detect changes in the biochemical markers, NADH and FAD, related to the progression of carcinogenesis. NADH and FAD are involved in redox reactions during cellular metabolism. This means that they are constantly binding to proteins and accepting electrons and or donating electrons. This leaves them in either a free or protein bound state where there will exist two populations, free and bound, of NADH and FAD within a cell. A commonly discussed feature is that NADH and FAD have a short and long lifetime corresponding to their free and protein bound state.[36] NADH will have a short lifetime if free, and a long lifetime if bound, with FAD exhibiting the opposite change. Not only do NADH and FAD have different lifetimes depending on their bound/free state, but the type of protein they are bound to and their surrounding environment can influence their lifetime. For example, a popular theory is that during carcinogenesis, the repertoire of NADH protein binding sites changes and results in a decreased lifetime for bound NADH.[37, 38] The primary cause of this phenomena is the shift in the type of metabolism that occurs with carcinogenesis. As the epithelial tissue begins to develop cancer, the

dominant metabolic pathway switches from oxidative phosphorylation to glycolysis.[39] There is also a relative decrease in the fluorescence contribution by protein bound NADH when comparing against free NADH, which could lead to lower lifetime readings if the free and bound NADH are not separately imaged.

Another phenomenon that occurs is that, in high grade dysplasia, there is a reduced presence of oxidized nicotinamide adenine dinucleotide (NAD+) that is postulated to increase the lifetime of protein bound FAD.[40] Other studies support this by showing that increased levels of NAD+ lower the lifetime of protein bound FAD.[40] In addition to the lifetime alterations of NADH and FAD during carcinogenesis, the collagen crosslinks in the lamina propria begin to break down as the epithelial cells start to invade. This results in a decrease in submucosal collagen fluorescence.[41] In short, collagen, NADH, and FAD can all be used to non-invasively monitor carcinogenesis and be used to differentiate pre-cancer and cancer from normal epithelial tissues.

1.7.2 Fluorescence lifetime measurement techniques

Several techniques exist to measure fluorescence lifetime, each with their own benefits and drawbacks. The techniques fall into two broad categories, the time domain and the frequency domain. Several methods exist to measure lifetimes utilizing these techniques, some being applicable in both.

1.7.2.1 Time domain FLIM

Time domain FLIM is the most conceptually simple to envision. The principle of time domain revolves around exciting the fluorophore of interest with a high intensity, ultra-short, pulse of light. This excitation light pulse is used to simulate an impulse

function to initiate the exponential decay of the fluorescence signal. Figure 1 shows how a standard fluorescence decay is measured in the time domain [33]. The pink Gaussian at t = 0 represents an impulse of excitation light. The purple emission curve represents the exponential decay of the emitted photons from the fluorophore.

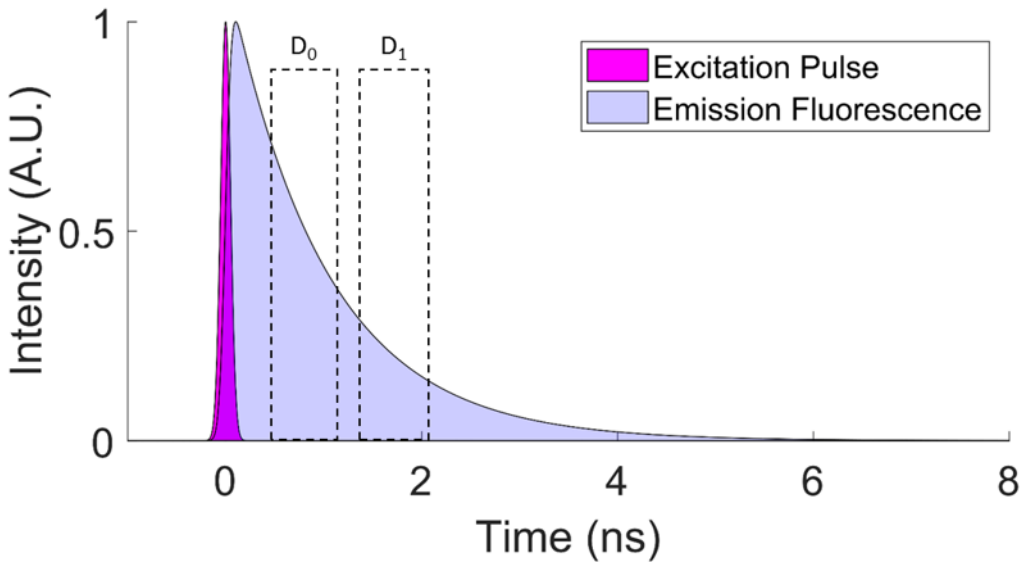

Figure 1 - Principle of time-domain lifetime measurement (see text). Fluorochromes are excited using a short pulse of light, after which the emitted fluorescence is measured time-resolved. Usually, fluorescence is recorded in two or more discreet time intervals represented here by D_0 and D_1, adapted from [33]

In principle, it is theoretically possible to measure the decay curve directly and fit it to an exponential function of the form found in Equation 2, where $I(t)$ is the intensity at time t relative to the excitation pulse, I_0 is the maximum intensity at $t = 0$, and τ is the rate constant (or lifetime).

Equation 2

$$I(t) = I_0 e^{(\frac{-t}{\tau})}$$

A common way to measure lifetime in the time domain is to use time correlated single photon counting (TCSPC). TCSPC records the arrival of photons relative to the excitation pulse and bins them to form a histogram which portrays an accurate representation of the fluorescence intensity emission decay curve. In order to ensure an accurate representation of the decay curve, the TCSPC detector must have a fairly low efficiency, ~5%, to ensure early photons are not over represented in the histogram [42]. Because of the low detection efficiency, TCSPC is generally very slow and not suitable for measuring lifetimes in dynamic biological samples; however, other time domain methods exist to fill this gap.

This work uses the rapid lifetime determination (RLD) method to quickly measure the lifetimes of fluorophores in dynamic media. RLD is generally a widefield imaging technique that uses a time gated intensified CCD camera (ICCD). These cameras have a microchannel plate (MCP) that can be time gated down to the sub nanosecond scale to allow sub nanosecond lifetime resolution. In Figure 1, each of the purple regions labeled D_0 and D_1 represent samples taken along the lifetime curve. Rather than measuring the curve directly, RLD integrates the intensity over a gate width and uses the ratio of the area under the decay curve in each gate to calculate the lifetime. This calculation can be seen in Equation 3 where τ is the lifetime, Δt is the gate width, and D_0 and D_1 are the respective areas under the curve for each gate.

Equation 3

$$\tau = \frac{-\Delta t}{\ln(\frac{D_1}{D_0})}$$

This simple formula only applies when the gates D_0 and D_1 occur sequentially with no delay between the two. More complicated gating schemes can be used but they require solving nonlinear functions [43]. For the purposes of this work, the standard RLD method was sufficiently fast and accurate.

1.7.2.2 Frequency domain FLIM

Although frequency domain FLIM was not used in this work, it is a widespread and useful technique for calculating lifetimes that warrants discussion. Frequency domain FLIM utilizes amplitude modulated excitation light to excite fluorophores and then measures the amplitude modulated emission spectra. Due to the probabilistic and non-instant emission of photons relative to the excitation light, the emission intensity will be phase shifted and scaled relative to the excitation light [33]. When considering using frequency domain FLIM, it is critical to ensure that the exact phase and modulation difference of the fluorescence signal can be measured relative to the excitation source. The basic concept of frequency domain FLIM can be easily derived from first principles. If it is assumed that the fluorescence decay of a fluorophore excited with an impulse follows as the solution to a first order linear time invariant system, the decay can be written as Equation 4 where $I(t)$ is the intensity, τ is the lifetime, and t is time.

Equation 4

$$I(t) = \frac{1}{\tau} e^{\left(\frac{-t}{\tau}\right)} \quad (4)$$

The modulated excitation source is convolved with Equation 4 to form the phase shifted emission intensity. The Fourier transform of Equation 4 can then be taken to determine the frequency phase response of the emission intensity (see Equation 5 where ω is the frequency of modulation, t is time, and τ is the lifetime).

Equation 5

$$I(\omega) = \int_0^\infty e^{(-i\omega t)} \frac{1}{\tau} e^{\left(\frac{-t}{\tau}\right)} dt = \frac{1}{(1 + i\omega\tau)}$$

The result of Equation 5 can be represented in polar form and is shown in Equation 6.

Equation 6

$$I(\omega) = \frac{1}{(1 + i\omega\tau)} = \frac{1}{\sqrt{1 + \omega^2\tau^2}} e^{(i * \arctan(\omega t))}$$

The real component of the exponential in Equation 6 shows the phase shift of the emission intensity relative to the excitation intensity while the pre-exponential factor shows the modulation shift.

Although frequency domain FLIM has less strict requirements for ultrashort pulsed lasers and ultra-fast detectors, new technology has eased the hardware restrictions on time domain FLIM, enabling it to be easily implemented.

1.8 Structured illumination microscopy

Because biological samples are often times much thicker than the depth of field (DOF) of a widefield microscope, and widefield microscopes possess no inherent optical sectioning capabilities, much of the in-focus information in an image is obscured by out of focus light [44]. It is therefore necessary to create samples thin enough to be wholly contained within the DOF, i.e. histological sections where a microtome is used to create

thin slices from a fixed tissue specimen on the order of ~5-10 μm [20]. Although this technique, especially when paired with stains such as H&E, provides an immense level of detail and allows for the precise evaluation of microscopic features in thick biological specimens, it is unable to provide live *in vivo* images. In order to image thick samples while preserving all spatial information, optical sectioning needs to be employed. Confocal microscopy was one of the first methods proposed to create optical sections and works by physically blocking out of focus light. The theory of confocal will be discussed in further detail later. Although confocal performs exceedingly well in thick tissue imaging, it is a point scanning technique which necessitates a tradeoff between imaging speed and field of view, both very important factors for *in vivo* biological imaging. Confocal can be made faster by decreasing pixel dwell time, lowering the system resolution, or increasing the excitation power, but other non-scanning, widefield, methods of optical sectioning may be a better alternative for fast video-rate biological imaging.

Structured illumination microscopy (SIM) is a powerful technique that can be used for optical sectioning. It is fundamentally simple to implement and can serve as a relatively inexpensive widefield optical sectioning alternative to point scanning methods such as confocal and two-photon microscopy. It can also be used for other imaging modalities such as super resolution microscopy, surface profiling, and phase imaging; however, we will only discuss optical sectioning in this work.[44]

1.8.1 History

Structured illumination as an optical sectioning technique was first feasibly introduced by Tony Wilson as a means of obtaining optical sections while using structured light in a conventional microscope.[45] It was initially proposed as an alternative to confocal microscopy that could be easily implemented on widefield microscopes. Throughout the years, further refinements have been made on the technique with some researchers implementing novel systems for creating modulated light (two beam interference, LED arrays, spatial light modulators, digital micro mirror devices, etc.) and others developing sophisticated error correction algorithms to account for optical aberrations and imperfect modulation phase shifts.[46-51] To this day, it remains a popular alternative to point scanning techniques.

1.8.2 Fourier imaging theory and sectioning in confocal microscopy

In order to understand how structured illumination creates optical sections, it is first useful to evaluate how confocal microscopy forms images and creates optical sections. Confocal microscopy can be thought of as a coherent imaging technique where all frequencies contained within the optical transfer function attenuate with defocus.[45, 52, 53] We first start by describing an electromagnetic field as a scalar field amplitude in Equation 7 where U is the complex field amplitude and ω is the angular frequency.

Equation 7

$$\overline{U} = Re\{Ue^{j\omega t}\}$$

One can then apply Kirchhoff's diffraction formula to derive the expression in Equation 8 where $k = 2\pi/\lambda$, λ is the wavelength, $U_2(x_2, y_2)$ describes the diffracted amplitude

given by the amplitude at the plane $U_1(x_1, y_1)$, and R is the distance between any two points on the planes.

Equation 8

$$U_2(x_2, y_2) = \iint_{-\infty}^{+\infty} \frac{1}{j\lambda R} U_1(x_1, y_1) e^{(-jkR)} dx_1 dx_2$$

After assuming that the axial distance between the planes is much larger than any lateral displacement between a point on the aperture in the first plane and the observation point on the second, Equation 8 can be simplified to Equation 9 where z is the perpendicular distance between the two planes.

Equation 9

$$U_2(x_2, y_2) = \frac{e^{(-jkz)}}{j\lambda z} \iint_{-\infty}^{+\infty} \frac{1}{j\lambda z} U_1(x_1, y_1) e^{(-\frac{jk}{2z}[(x_2 - x_1)^2 + (y_2 - y_1)^2])} dx_1 dx_2$$

Again if we impose the restriction to $z \gg (1/2)\mathrm{k}(x_1^2 + x_2^2)$, we can simplify Equation 9 to what is known as the Fraunhofer approximation shown in Equation 10.

Equation 10

$$U_2(x_2, y_2) = \frac{e^{(-jkz)}}{j\lambda z} e^{\left(-\frac{jk}{2z}(x_2^2 + y_2^2)\right)} \times \iint_{-\infty}^{+\infty} \frac{1}{j\lambda z} U_1(x_1, y_1) e^{(\frac{jk}{z}[x_1 x_2 + y_1 y_2])} dx_1 dy_1$$

Using the Fourier transform on Equation 10, a relationship between the amplitude at the observation plane and the Fourier transform of the diffracting aperture can be found, see Equation 11 where $\widetilde{U}_1$ is the Fourier transform of the aperture plane.

Equation 11

$$U_2(x_2, y_2) e^{\left(\frac{jk}{2z}(x_2^2 + y_2^2)\right)} = \frac{e^{(-jkz)}}{j\lambda z} \widetilde{U}_1(\frac{x_2}{\lambda z}, \frac{y_2}{\lambda z})$$

Equation 11 can then be used to approximate a lensless imaging system functioning in the Fraunhofer realm.

To analyze familiar imaging systems, it is then useful to evaluate the effects of lenses on an imaging system within the context of Fourier imaging theory. Lenses can be modeled as a circular aperture that imparts a spatially varying phase shift on an incident field. This phase shift results in a plane wave being converted into either spatially diverging or converging spherical waves. Equation 12 defines the phase function of a lens where f is the focal length.

Equation 12

$$t(x,y) = e^{(\frac{jk}{2f}(x^2+y^2))}$$

Combining Equation 12 with Equation 11 and the pupil function gives us Equation 13 where a is the aperture radius, r_2 is the radial distance at the focal plane, $v = 2\pi r_2 a/\lambda f$ is the normalized optical coordinate, and $N = (\pi a^2/\lambda f)$, more commonly known as the Fresnel Number.

Equation 13

$$U_2(v) = -jNexp^{(-\frac{jv^2}{4N})}\frac{2J_1(v)}{v}$$

Equation 13 can be thought of as the complex amplitude in the focal plane as the normalized radial coordinate is varied. It is well known that intensity is defined as the squared modulus of the amplitude for optical system. Taking this into consideration, the intensity in the focal plane is then proportional to $[2J_1(v)/v]^2$ and gives form to the point spread function $h(v)$. Figure 2 plots the point spread function in terms of intensity and normalized radial position in the focal plane.

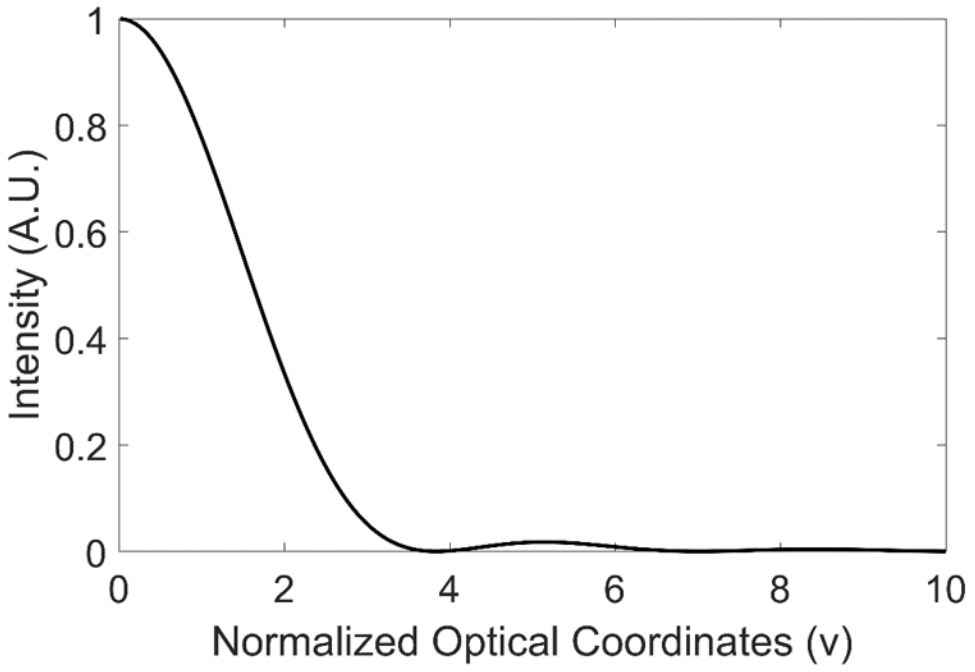

Figure 2 - Lateral point spread function. Intensity distribution in the focal plane of a circular lens, adapted from [53]

Now that we have established image formation at a basic level, we can evaluate image formation with defocus to glimpse at how confocal microscopy optically sections. To determine the effects of defocus on the system, which will determines the system's optical sectioning capabilities, Equation 13 needs to be recreated to account for displacement from the focal plane. When simplifying from Equation 10 to Equation 13, several terms in the numerator are cancelled out because *z* is equal to *f*, i.e. imaging at the focal plane. We must now use Equation 14, which is generalized to account for axial displacement. In Equation 14, α is the half angle formed by the pupil and the image plane, $u = 4k\delta z sin^2(\alpha/2)$ is then the normalized axial coordinates, and $\rho = r_1/a$ is

the normalized pupil radius. Equation 14 is only valid when the displacement from the focal plane is very small.

Equation 14

$$U_2(u,v) = -jNexp^{(-jkz)}exp^{(\frac{-jv^2}{4N})}\int_0^1 2e^{(\frac{1}{2}jup^2)}\frac{J_0(\rho)}{\rho}d\rho$$

Equation 14 represents the amplitude in both the radial and axial direction. Again if we take the modulus and square it, the point spread function for the lateral and axial directions can be abstracted. Equation 15, where $P(\rho)$ is the pupil function for a given circularly symmetric aperture, represents the three dimensional point spread function. [54]

Equation 15

$$h(u,v) = \int_0^1 P(\rho)e^{(\frac{1}{2}jup^2)}\frac{J_0(\rho)}{\rho}d\rho$$

For a confocal microscope that shares an illumination and imaging path, the intensity at the detector can be written as Equation 16 where D the detector radius, defined as $circ(v/v_p)$ where v_p is the radius, and * is the convolution operation. It should also be noted that a confocal microscope is theoretically a coherent imaging system if there is a point source and point detector. This would imply that image formation would sum in complex amplitudes before being squared to give an intensity. In practice, confocal microscopes have some physical aperture size of the detector that limits this and are considered partially coherent. Equation 16 is valid when imaging a point object with a system that has a finite aperture D.[54]

Equation 16

$$I(u,v) = |h|^2(|h|^2 * D)$$

Although analyzing a point source is useful in describing the effects of defocus when imaging with a confocal imaging system, the true power of a confocal imaging system is revealed by considering the effects of imaging an extended source.[55] In fact, for a point source, a widefield imaging system only has a worse axial resolution by a factor ~2. This means that although worse than confocal, a point source will eventually be attenuated by a conventional widefield imaging system and no longer be visible. Conversely, an extended source will be imaged in two very different ways. When the source is in focus, both imaging modalities behave relatively similarly, again, with confocal possessing slightly better resolution in all dimensions. However, as the extended source goes out of focus, one can see that the intensity for confocal devices vanishes rather quickly while the intensity for a conventional widefield imaging system tends towards a uniform background. This stems from the inability of the conventional widefield instrument to attenuate the zero spatial frequency. Plotting the intensity of the zero spatial frequency for both modalities would reveal a function that decays with defocus for confocal and a horizontal line without decay for conventional widefield. It should be noted that higher spatial frequencies in the conventional method still attenuate with defocus, a critical factor that will play into generating optical section with structured illumination microscopy. Further exploration into confocal optical sectioning can be made, but Equation 17 can be used to calculate the practical optical section thickness of a given confocal microscope.[54, 55]

Equation 17

$$I_{plane}(u) = \int_0^{v_p} |h(u,v)|^2 v dv$$

$$= \left[\frac{\sin(\frac{u}{2})}{(\frac{u}{2})}\right]^2, \qquad when\ v_p = 0$$

1.8.3 Structured illumination imaging theory

Structured illumination and its ability to optically section can be easily explained by drawing parallels to confocal microscopy and discussing the key features that are different between them. One of the most notable differences that must be accounted for is that structured illumination microscopy is a widefield modality and is generally considered an incoherent imaging technique, while confocal is generally considered a coherent imaging technique. As previously discussed, this means that the image formation does not occur as a linear summation of complex amplitude, but rather linear summation of the squared modulus of the amplitude. In image theory, this is referring to whether or not the point spread function is squared before or after convolution with the object. Unlike coherent imaging techniques, incoherent imaging techniques possess no inherent optical sectioning capabilities. So the question then becomes: if incoherent imaging techniques possess no inherent optical sectioning capabilities, how do we generate optical sections? The answer to this question can be found by looking at the axial point spread function and, by extension, the axial optical transfer function.

To help give context to a mathematical evaluation of this problem, it is helpful to sketch a simple structured illumination imaging system. Generally a fringe pattern is

projected into the sample plane for structured illumination, but for this simple analysis a fringe pattern is considered to mysteriously exist in our sample.

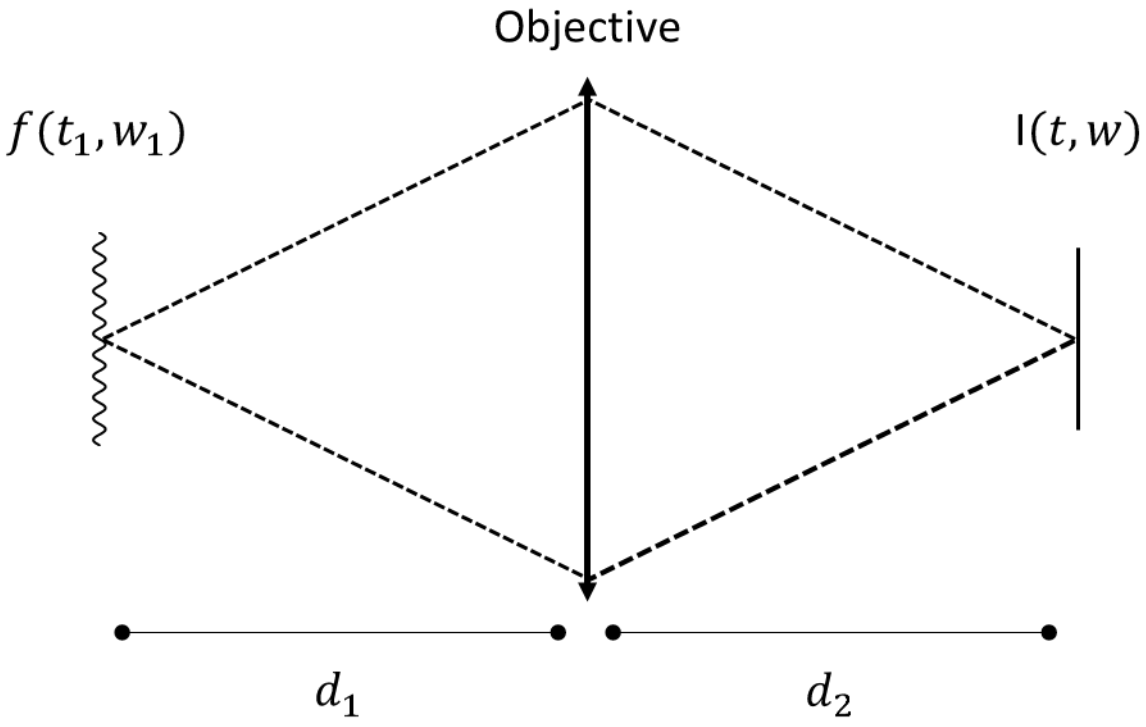

Figure 3 - Simple imaging system with a fringe pattern in the focal plane, adapted from [56]

Figure 3 shows a simple imaging setup where a single lens is imaging a fluorescent object with a fluorophore distribution $f(t_1, w_1)$ where t and w are the normalized lateral optical coordinates found by $(t, w) = (\frac{2\pi}{\lambda})(x, y)nsin\alpha$. Here $nsin\alpha$ is the numerical aperture of the objective and λ is the wavelength of light.

We can say that the fluorophore is illuminated by one-dimensional intensity pattern shown in Equation 18 where m is the modulation depth of the cosine amplitude, ϕ is the phase of the cosine function, and g is the normalized spatial frequency of the cosine function.

Equation 18

$$I_{excitation}(t_1, w_1) = 1 + m * \cos(gt_1 + \phi)$$

In a fully realized system Equation 18 can be thought of as the illumination pathway that is projecting a fringe pattern into the sample. However, the following analysis will consider the illumination to be formed from a coherent interference pattern illuminating the sample. This simplifies the analysis, but still allows one to evaluate the driving principles behind structured illumination microscopy and its ability to optically section. Another point to consider is that although the illumination light is coherent, the emitted fluorescence is wholly incoherent across the field of view and creates an incoherent imaging system.[56] The emission light can then be represented by Equation 19, which is simply a multiplication of the excitation light and fluorescent object.

Equation 19

$$I_{emission}(t_1, w_1) = [1 + m * cos(gt_1 + \phi)]f(t_1, w_1)$$

The image formed at the detector can be represented by the intensity point spread function, $|h|^2$, of the objective convolved with the emission light, seen in Equation 20.

Equation 20

$$I(t, w) = \iint [1 + m * \cos(gt_1 + \phi)]f(t_1, w_1)|h(t + t_1, t + w_1)|^2 dt_1 dw_1$$

$I(t, w)$ now represents an image of the fluorescent object in the focal plane modulated by a sinusoid with some spatial frequency. This integral can be broken down into its

component parts which consists of an unmodulated image and a frequency modulated image. Equation 21 presents a basic form of the summed terms taken from Equation 20.

Equation 21

$$I(t,w) = I_{dc}(t,w) + m * I_m \cos(2\pi g x + \phi)$$

I_{dc} has the same mathematical form that would be consistent with a plane wave illuminating a fluorescent sample in an incoherent imaging system. It can be thought of as a DC background image upon which our modulated terms are added. I_m represents the intensity of the sinusoidal modulated image. Evaluating how I_{dc} and I_m behave with defocus reveals the underlying principle behind structured illumination's ability to optically section.

The simplest representation of SIM's optical sectioning can be made by plotting the attenuation of different normalized spatial frequencies, υ, as a function of axial defocus from the system focal plane.[56] The attenuation follows the form of a first order Bessel function divided by its input and is very similar to confocal attenuation in Equation 17.

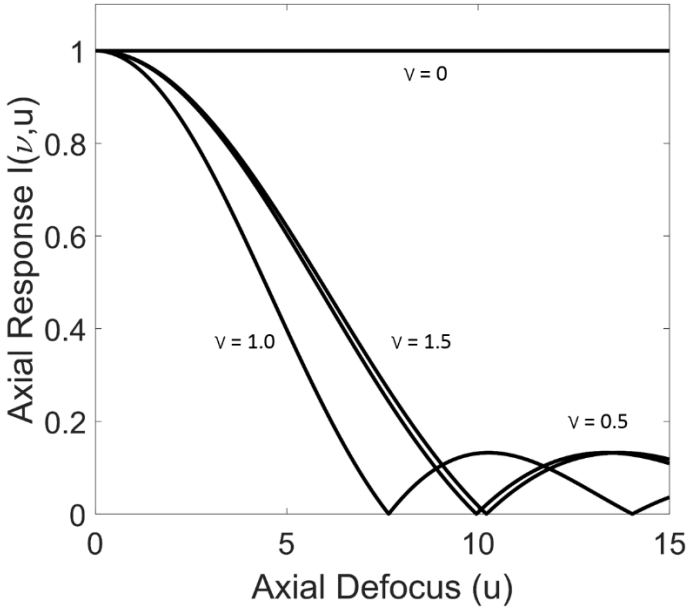

Figure 4 - Spatial frequency attenuation with axial defocus. Axial units are normalized optical units (u) and the different lines are normalized spatial frequency (ν), adapted from [56]

Figure 4 gives an accurate representation of the effects of defocus on spatial frequencies within SIM imaging system. The ordinate describes the intensity and the abscissa describes the normalized distance away from the focal plane. The different lines in Figure 4 represent different spatial frequencies within the image. As can be seen, the normalized spatial frequency υ = 0.0 corresponds to a typical case of a non-sectioning widefield imaging microscope where the DC level from all axial locations is present within the image formed by the system. We can also see that different frequencies such as υ = 1.0, 1.5, and 0.5 do attenuate with defocus. This means that information with these spatial frequencies does not appear in planes other than the one currently in focus.

It then follows that if one modulates content in the focal plane with a spatial frequency that attenuates with defocus, one can retrieve that information and create an optically sectioned image. The goal is to recreate an image represented by Equation 21 in terms of I_m while simultaneously removing I_{DC} and any residual modulation. This can be done using a three phase demodulation technique. First the focal plane is illuminated with a modulation pattern in the form of a sinusoidal varying pattern such as that shown in Equation 21. Three images are taken with each subsequent image phase shifted a third of a period relative to the previous image (0, 2π/3, and 4π/3)

Equation 22

$$I_{sectioned} = \sqrt{(I_1 - I_2)^2 + (I_2 - I_3)^2 + (I_1 - I_3)^2}$$

Equation 22 shows the algorithm used to calculate a sectioned image, $I_{sectioned}$, where $I_{1,2,and\ 3}$ are the three phase shifted images. Utilizing this method, optically sectioned images can be generated using a widefield imaging system.

CHAPTER II

VOLUMETRIC STRUCTURED ILLUMINATION ENABLED BY A TUNABLE-FOCUS LENS

2.1 Introduction

As previously mentioned, optical sectioning in high-resolution microscopy is often desirable to improve resolution and contrast. A number of point-scanning optical imaging techniques, such as scanning confocal and multiphoton microscopy, are capable of providing optical sectioning by eliminating out-of-focus light.[52, 57] A full 3D volume containing information about a thick samples can be generated by scanning in depth. A widefield alternative to provide optical sectioning is SIM, wherein typically three or more images are acquired at preset spatially offset illumination patterns, and out-of-focus light is rejected by mathematical manipulation of the acquired images.[45]

In most common embodiments of optical imaging systems, a single in-focus image can be acquired quickly. However, the 3D volumetric acquisition, which requires refocusing to successive image planes, is relatively slow and is one of the limiting factors toward high-speed volumetric image acquisition. More recently, variable-focal-length lenses have seen considerable utilization towards axial scanning in a multitude of optical-imaging modalities.

These include high-resolution imaging techniques, such as multiphoton, confocal, and light-sheet microscopy, as well as optical projection tomography.[32, 58-62] Our group recently reported the use of an electrically tunable lens (ETL) to provide axial scanning in a reflectance confocal microscope and also demonstrated its application and benefits in a clinical device. [60, 63]

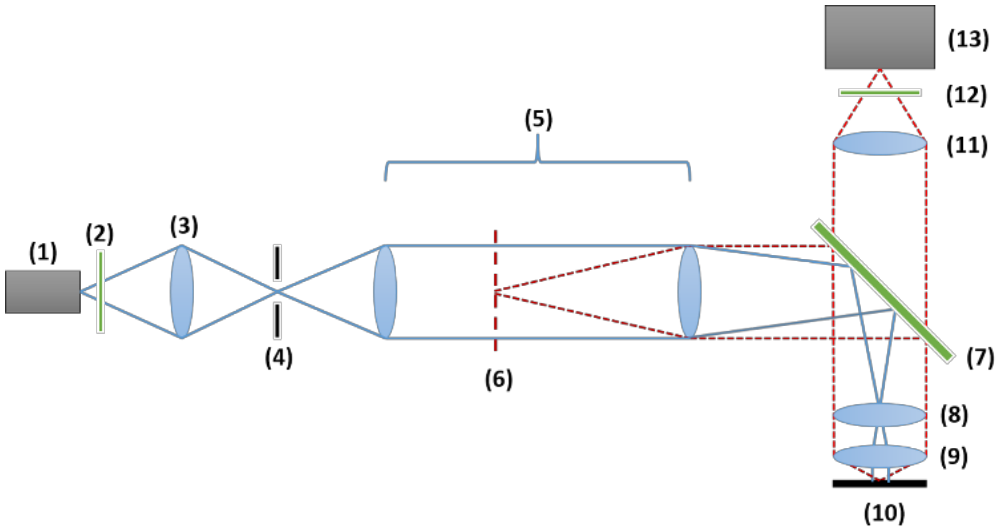

Figure 5 - SIM system schematic. (1) LED, (2) Excitation filter, (3) Condenser lens, (4) Condenser aperture, (5) Image relay, (6) Ronchi ruling, (7) Dichroic mirror, (8) Tunable lens, (9) Objective lens, (10) Sample plane, (11) Tube lens, (12) Emission filter

Here, we present the use of a commercially available ETL wherein the focal length can be varied as a function of the supplied electrical signal to achieve axial scanning in SIM. To the best of our knowledge, this is the first reported of the use of a

variable-focal-length lens in SIM for imaging biological tissue. We have characterized the optical properties of our SIM, incorporating an ETL and quantified lateral resolution and axial response over the axial scan range of the system. The performance was further demonstrated by imaging of fresh tissue samples from bovine oral mucosa *ex vivo*.

2.2 System

Our SIM system is based on a conventional widefield geometry utilizing a Ronchi ruling for patterned illumination and an ETL placed just before the objective to enable axial scanning. Figure 5 shows the experimental setup of the system. The system consists of a Kohler illuminated epi-fluorescence microscope. A condenser lens (ACL2520A, Thorlabs, Newton, New Jersey) collects the light from the 455 nm light emitting diode (LED) source (M455L3, Thorlabs) and forms an image on a restricting iris. An image relay (AC254-040-AML, AC254-150-ML, Thorlabs) is used to focus the light to the rear focal plane of the objective [40×, numerical aperture NA 0.66, Achromat, Leica]. The fluorescence emitted from the sample is imaged onto a CCD camera (ExiBlue, QImaging, Surrey, BC, Canada) via a 200 mm focal length tube lens (AC254-200-A-ML, Thorlabs). The excitation light is spatially modulated via a 20 line pairs/mm Ronchi ruling (58- 777, Edmund Optics, Barrington, New Jersey), which is placed in the middle of the 4f system, conjugate to the focal plane of the objective lens, with a magnification between the ruling plane and the object plane of 1/30. The Ronchi ruling is mounted on a translation stage (T-LSM100A, Zaber, Vancouver, Canada) to enable horizontal movement. To provide axial scanning, the ETL (EL-10-30, Optotune, Switzerland) is placed as close as possible to the rear focal plane of the objective. A

450/20 nm excitation filter (FB450-40, Thorlabs), a 500 nm long pass emission filter (FELH0500, Thorlabs), and a 490 nm cutoff dichroic mirror (DLMP490R, Thorlabs) are used to separate the fluorescence emission from excitation light.

2.3 Methods, Results, and Discussion

Fresh bovine oral epithelial tissue was acquired from a local butcher shop. Acriflavine hydrochloride (Sigma-Aldrich, St. Louis, MO) was used as a fluorescent contrast agent to stain and visualize the epithelial nuclei. Up to 1 mL of acriflavine solution (0.01% w/v in sterile phosphate buffered saline [PBS]) was applied topically to the tissue with a cotton-tipped applicator for 1min, rinsed in sterile PBS solution, and imaged immediately. While acriflavine is not yet approved by the US Food and Drug Administration for internal use in the oral cavity, it has a long history of safe clinical use as a topical antiseptic agent and as a fluorescence contrast agent for endomicroscopy [64].

After tissue preparation, the samples were imaged using standard SIM methodology. Three images were taken with the grid pattern shifted one-third of a period relative to the last frame in succession. Combining these images with the SIM phase demodulation technique described in the introduction section removed out-of-focus light and produced optically sectioned images with enhanced signal-to-background ratio.

To test the capabilities of our system, 200 nm subresolution fluorescent microspheres on a thin film were imaged to measure both the lateral resolution and the axial response. Increasing curvature of the ETL is known to increase spherical aberration

[60]. To evaluate the effect of the ETL on image quality, measurements of the axial response, the lateral resolution, and the field of view (FOV) were taken over the full

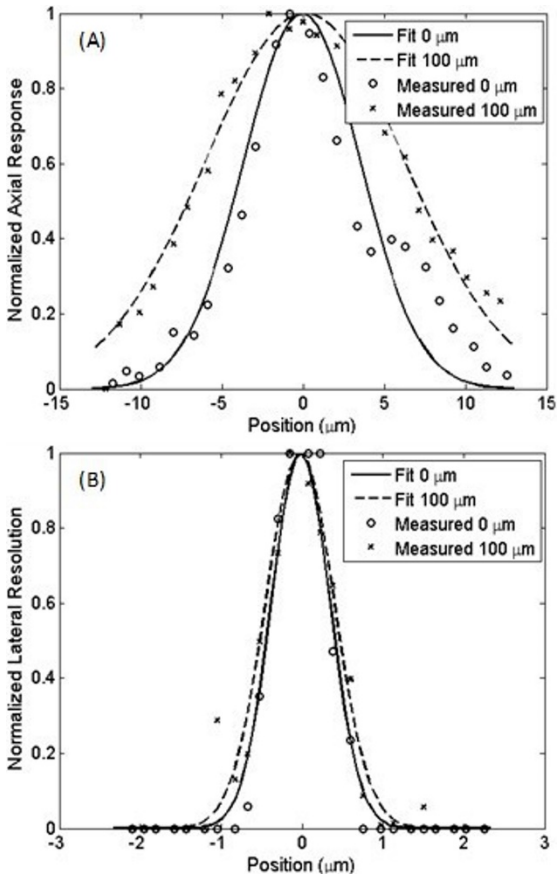

Figure 6 - (A) Axial response of SIM at 0 µm and 100 µm scan distance. Using a Gaussian fit, the full-width-half-maximum, FWHM of the axial response is 7.95 µm and 14.13 µm, respectively. (B) Lateral resolution of optical system at 0 µm and 100 µm scan

range of the axial scan (100 µm), where the ETL scans through a focal length range from 130 mm to 90 mm, corresponding to microscope focal positions defined as 0 µm and 100 µm, respectively. Figure 6 shows the measured axial response (top) and the lateral

resolution (bottom) at the distal scan position, where the focal length of the ETL is set to its maximum of 130 mm, and the proximal focal position, where the ETL focal length is 90 mm.

The measurements were made on single spheres near the center of the FOV and normalized by their maximum intensity. For the axial response, the average intensity of a sphere was plotted as it was axially scanned through the focus. As mentioned in the introduction, using beads may have overstated the optical sectioning thickness. However, the spheres were often very close in proximity and blurred together with defocus. For the lateral resolution, the line profile of the sphere at optimum focus was plotted. The FOV and magnification were measured by imaging a Ronchi ruling and then determining the pixels per line pair.

To evaluate this data over the full scan range, the axial response, the lateral resolution, the FOV, and the magnification were measured at three scan positions across the full tunable range, starting with the ETL focal length set at 130 mm, which minimizes the displacement of the focal position from the objectives' nominal working distance. This position is called the 0 μm focal position and is followed by subsequent scanning up to 50 μm and 100 μm in depth. We expected a theoretical axial response of 7.94 μm and a theoretical diffraction limited lateral resolution of 0.46 μm. The expected axial response is calculated using a spatial frequency response curve that considers the magnification between the grid plane and the sample plane. Using parameters from the physical system, the actual axial response can be numerically calculated [4]. The difference between the expected and measured lateral resolution can likely be attributed

to the use of an ETL and, to some degree, the achromatic objective, which introduces additional spherical aberrations. A changing system NA throughout the scan range is another possible cause of the enlarged lateral resolution. Even at the zero scan position, there is still an offset from the nominal working distance, thus an altered NA. The physical size, 200 nm, of the measured microspheres would also affect the lateral resolution. Although they are subresolution, they are not perfect point sources. The measured values are reported in Table 1.

The change in the FOV is caused by the ETL not being placed in the pupil plane of the objective as mentioned earlier. A Zemax model was created to estimate the theoretical shift in focal plane and change in magnification. It consisted of a generic 40× (5 mm focal length) microscope objective model, an official ETL model, and a model of the tube lens used in our system. All these elements were arranged and optimized to be separated from each other with the same distances as in the physical system. Table 1 shows the measured magnification range from 30.5 to 36.2. Using the Zemax model that had the ETL placed 25 mm from the pupil plane of the objective, just as in the physical system, it was shown that over the change in curvature used to scan in our system, the magnification changed from 32.53 to 35.92. Over this full scan range, the focal position exhibited a displacement of 98 μm, which is in relative agreement with the measured 100 μm for the maximum relative displacement. The small differences can likely be attributed to using a generic objective lens model instead of the actual model, which is not provided by the manufacturer. If a lens relay is placed in the Zemax model to image the pupil plane of the objective onto the ETL, the magnification change is greatly

reduced. With this simple relay model, it was shown that the magnification changed less than 0.95% over the whole scan range. This can be potentially incorporated in a future system.

Table 1 - Focal position (FP), Axial response (AR) mean (st. dev), lateral resolution (LR) mean (st. dev), field of view (FOV), and magnification (M)

FP (μm)	0	-50	-100
AR (μm)	7.95 (0.84)	10.55 (1.56)	14.13 (0.22)
LR (μm)	0.78 (0.1)	0.93 (0.08)	1.14 (0.19)
FOV (μm2)	248 × 185	268 × 200	293 × 219
M	30.5	33.4	36.2

To demonstrate the application of our technique in biological tissue, nuclear imaging in bovine epithelial tissue was performed *ex vivo*. The focal plane was axially scanned 100 μm (equivalent to 133 μm when accounting for the refractive index of water in tissue) in depth using the ETL. The scan was performed only in one direction and returned to the starting position at the end of the scan, essentially replicating a sawtooth profile. A maximum intensity projection (MIP) was made over the acquired image stack to show all the in-focus content in the series. Figure 7 shows the MIP images for both the widefield (top) and the SIM-processed (bottom) data. Note that when referring to the widefield images, they are constructed by averaging the three structured illumination images, which mathematically represents a widefield image.

The difference between the SIM-processed images and the widefield images is apparent in Figure 7. The details of the stained nuclei and tissue is preserved much better in the SIM MIP when compared with the widefield MIP; however, this is a qualitative comparison.

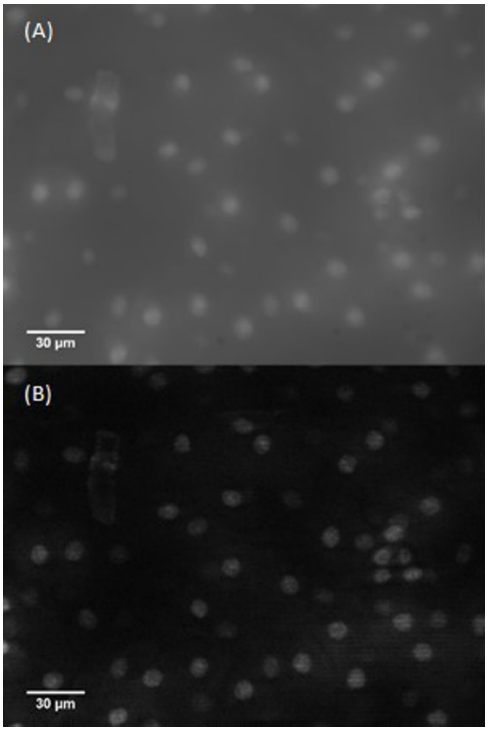

Figure 7 - Comparison of (A) widefield microscopy and (B) SIM image of oral mucosa stained with acriflavine; Both A and B are MIP images created from 133 µm axial scan using an ETL and (Media 1) raw image stacks.

Multiple cell layers can also be resolved in the image stack as seen in Figure 7. Note Figure 7 does not account for changes in magnification across the axial scan range. While this did not significantly affect the MIP images for qualitative observation, the

varying magnification would need to be taken into consideration for a quantitative feature analysis. The penetration depth was also limited in this experiment by the lack of dye penetration deep into the tissue. Topical acriflavine has been shown to have limited penetration and stain only the first couple of superficial epithelial cell layers and have no penetration into deeper layers such as the lamina propria.[65, 66] Although the scan range covers a distance 100 μm, features are only resolvable over the first two cell layers, corresponding to an imaging depth between 15 and 20 μm.

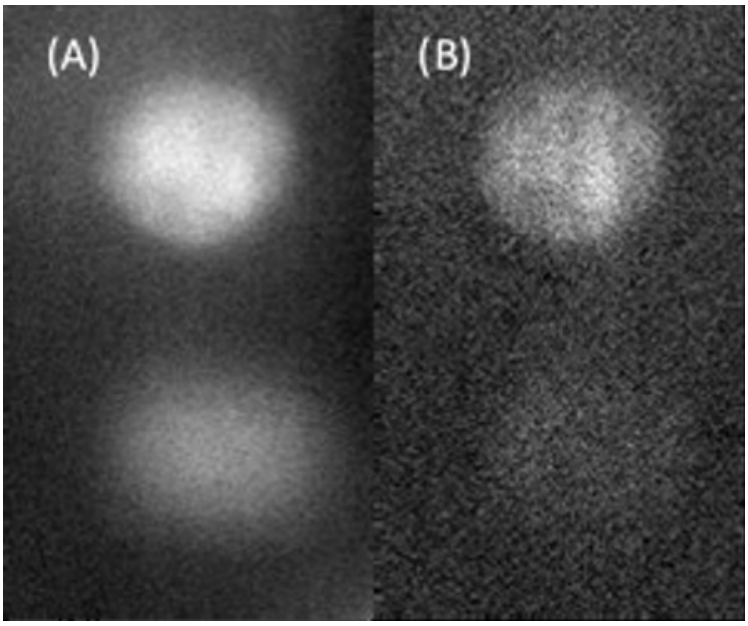

Figure 8 - (A) Single image slice without SIM processing of an in focus nucleus (top) and an out of focus nucleus (bottom) in acriflavine stained oral mucosa. (B) Following SIM, the out of focus nucleus is significantly removed.

Figure 8 shows a close-up view of the effects of SIM processing on in-focus and out-of-focus nuclei from a single image slice. It is clearly seen that out-of-focus nuclei are removed from the image. The SIM images and widefield images in Figure 8 were normalized with the same procedure, subtracting the background and scaling the maximum intensity to span the whole dynamic range, to ensure the relative intensities of the in-focus to out-of-focus nuclei could be compared across images. The ratio of the intensity of the in-focus nuclei to the out-of-focus nuclei in Figure 8 (A) improved from 1.62 to 2.35 in Figure 8 (B). This shows an improvement in optical sectioning by rejecting signal from the out-of-focus region.

The advantage of this SIM system with the ETL is that it can create optical sections and scan axially without any mechanical means. This provides the microscope with greater flexibility for *in vivo* use and the potential to be incorporated into an endoscopic system, especially with the advent of smaller tunable lenses.[67] Note that SIM has also been used for resolution enhancement. This can be achieved by increasing the number of structured illumination patterns at different orientations and phases. While the current optical resolution of our presented imaging system is adequate for tissue-level imaging, it can be potentially further increased for subcellular imaging.[68]

One drawback of using ETLs is that typically they are not well corrected for aberrations at all focal lengths across the scanning range, which can lead to reduced and varying image quality with greater curvature, resulting in discrepancies in theoretical and measured parameters. The ETL also introduced slight magnification errors, which can be seen as a change in the FOV in Table 1. As mentioned earlier, this is due to the

ETL not being in the rear focal plane of the objective. In addition, any change in divergence or convergence of the beam (by tunable lens) changes the effective NA of the system, potentially contributing to the disagreement in modeled and measured values of optical resolution. This can potentially be solved by using an image relay to image the rear focal plane of the objective onto the ETL.[58]

The acquisition of phase-shifted images in our system requires movement of the Ronchi ruling, which is the limiting factor in our image grid translation accuracy. Imperfect translations of the Ronchi ruling can result in images not shifted by exactly one-third of a period, resulting in image artifacts after SIM processing. To address this problem, the translating grid pattern can be replaced with a digital micromirror device (DMD) that utilizes a digitized displacement rather than analog.[69] The grid translation rate at ~40 Hz was not a limiting factor for our imaging rate of 0.5 Hz; rather, the exposure time was. The optical layout used in this here is specific to this system but the principle of the ETL scanning is easily generalizable to fit most widefield optical imaging systems.

In summary, we have presented an all optical axial scan method to provide volumetric imaging using SIM within biological tissue. Employing a tunable-focal-length lens can offer a more versatile mechanism for axial scanning within the sample with no relative motion of the microscope objective. In addition, the commercially available tunable lens can be easily retrofitted on most custom-built widefield microscopes with minimal system changes, or it can be added in a conjugate image plane in more restrictive commercial microscopes.

CHAPTER III

OPTICALLY SECTIONED WIDEFIELD FLUORESCENCE LIFETIME IMAGING MICROSCOPY ENABLED BY STRUCTURED ILLUMINATION

3.1 Introduction

We have so far shown that SIM could be used *ex vivo* in thick epithelial sections. Our next aim was to prove that the both SIM and FLIM could be combined and used to image distinct fluorescent layers in tissue models. FLIM has been extensively discussed in the introduction to this thesis, but a brief review is contained in the following text.

FLIM is a widely studied imaging modality that is most commonly used for its ability to distinguish multiple fluorophores of similar spectral characteristics, thus allowing for the chemical analysis of microscopy samples via both their fluorescence spectral and temporal properties. It is particularly attractive because it allows for high resolution spatial analysis of chemical distributions with little to no dependence on the intensity of the fluorophores under scrutiny.[36]

When considering biomedical applications, it is important to choose a FLIM modality that can function effectively *in vivo*. The widefield imaging approach is well suited for this task because it theoretically allows for the rapid measurement of fluorescent lifetimes at greater than 2 frames per second, while maintaining a relatively large field of view.[22]

In contrast to other FLIM methods that are typically based on laser scanning techniques, widefield imaging helps decouple field of view from imaging speed, allowing for faster acquisition that is less susceptible to motion artifacts, a necessity for *in vivo* FLIM.

However, FLIM suffers adversely from the effects of out of focus light where background contributions to the intensity can lower the measured fluorescence lifetime contrast between layers and lead to incorrectly calculated lifetime values.[70] Multiple exponential fitting methods exist to alleviate the problems that occur with spatially overlapping intensities, but these generally lengthen acquisition by requiring more than two gates and complicate the lifetime calculation processes.[71] A potentially simpler method is to separately image the intensities in the focal plane while minimizing contributions from the background with the use of optical sectioning techniques. Several optical sectioning techniques have been implemented in conjunction with FLIM such as two-photon, confocal, and structured illumination microscopy.[33, 72] We utilize SIM instead of other sectioning alternatives as it provides a means to optically section with a widefield imaging modality, an important consideration for *in vivo* application.

Although SIM has been shown to be able to provide accurate lifetime measurements when used in conjunction with FLIM, accurately resolving multiple layers with different lifetimes in thick samples such as tissue has yet to be demonstrated.[72] A major aim of the research presented herein is to be able to differentiate the fluorescence signal originating from the oral epithelium, where the bulk of the fluorescence signal is known to be associated with FAD and NADH, from that of the underlying collagen-

containing submucosa. We aim to demonstrate that this technique can be used for imaging fluorescence lifetime in relatively thick tissue samples such as oral epithelium.

3.2 Materials and methods

3.2.1 SI-FLIM system design

To measure fluorescence lifetimes with sectioning capability, we constructed a standard widefield epi-fluorescence microscope. Figure 9 shows the layout of the SI-FLIM system. An 800 ps pulse width, 355 nm wavelength, laser (AOT-YVO-100QSP/MOPA) operated at 6.25 kHz is coupled into a 400 μm core fiber via a 100 mm focal length lens (LA4380, Thorlabs). The laser delivered an average power of 1 mW to the sample with a peak power of 176 mW. The 400 μm core fiber was chosen because it allowed a pseudo flat-top super Gaussian illumination profile. The fiber is attached to a galvanometer scanner motor and vibrated to reduce the effects of laser speckle and mode patterns. A 50 mm lens (LA4765, Thorlabs) is used to collimate the output of the fiber to fill the full aperture of a DMD, digital micro mirror device, (DLi D4100, DLi) window with 1024x768 resolution and 13.68 μm pixel pitch. Using 24 pixels per line, resulting in a modulation frequency of 30.45 lines per mm at the sample. Light from the DMD is then spatially filtered using two 50 mm focal length lenses (65-976, Edmund Optics) and an iris to pass only the 0^{th} diffraction order; this helps maintain good contrast of the DMD pattern. A 100 mm field lens (65-979, Edmund Optics) then relays the illumination intensity to the rear focal plane of the 20 × objective (N20X-PF, Thorlabs). The objective is placed so that the DMD is in a conjugate image plane relative to the objective focal plane, while the image of the light source is in a Fourier plane.

A dichroic beam splitter (FF365-Di01-25x36, Semrock) is used in conjunction with three different emission filters to separate the image intensities into three separate spectral bands: 390 nm +/– 20 nm (86-348, Edmund Optics), 450 +/– 20 nm (FB450-40, Thorlabs), and 550 +/– 16 nm (BrightLine550-32, Semrock). The fluorophores associated with these emission bands are collagen/POPOP, NADH, and FAD, respectively. The emission filters are mounted in a slip mount (SMQ1P, Thorlabs) so that they can be quickly swapped with one another into the beam path. The tube lens (ITL200, Thorlabs) then forms an image on the ICCD camera (4Picos, Stanford Computer Optics). The ICCD camera can be gated and delayed with at temporal resolution of 200 ps. The gates chosen were specific to the expected lifetimes being measured with the gates for POPOP, NADH, and FAD being 1.3 ns, 0.5 ns, and 2.5 ns, respectively. The camera is set to trigger off of a high speed photodiode (SV2, Thorlabs) that reads light from a ~95/5 beam splitter (BSF10-UV, Thorlabs) pick off placed just after the laser output and before the coupling lens. This method ensures that the camera is always triggered relative to the actual output of the laser pulse and helps to minimize the effects of jitter.

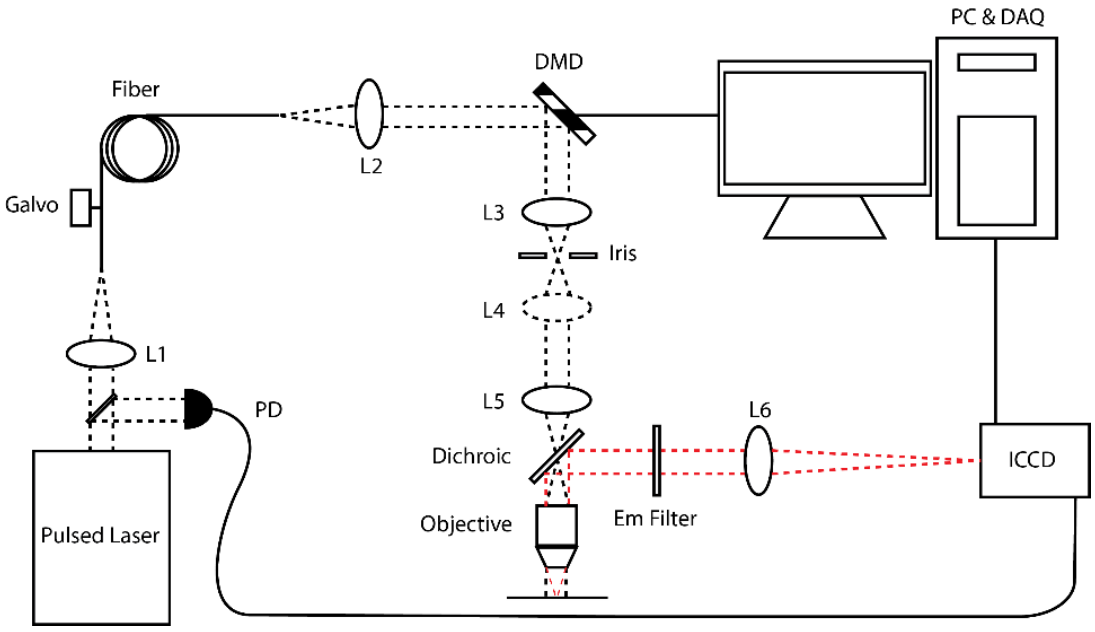

Figure 9 - SI-FLIM system schematic. L1: fiber coupling lens; L2: collection/collimation lens; L3/L4: 1:1 spatial filter lens pair; L5: field lens; L6: tube lens; ICCD: intensified CCD camera; PD: photodiode. Black dashed lines represent the field; red dotted lines represent the image

3.2.2 SI-FLIM computational methods

For our system, we used the RLD method, where two gates are used to determine the lifetime of the sample [43]. The RLD method functions by integrating the area under the lifetime decay curve, which yields an intensity image. If two gates are taken with one starting from the peak of the decay curve and the other delayed by the width of the gate, the lifetime can be calculated using Equation 3. Certain limitations apply to this method, i.e. one must know the general lifetime ranges trying to be measured to appropriately set the gate width and minimize noise [43]. In addition, if multiple lifetimes are present in a

single pixel, the RLD method will yield an average lifetime value; however, implementing optical sectioning techniques would potentially reduce these effects.

Structured illumination provides optical sectioning capabilities by using a spatially modulated illumination profile. Generally, a sinusoidal varying pattern is projected onto the sample as shown in Equation 21. This is usually approximated as a binary bar pattern using a simple Ronchi ruling in the illumination path, or in this system, a DMD. The DMD offers the benefits of being able to digitally control the phase of the grid pattern with a level precision not easily accessible to analog devices such as linear stages. The fluorescence signal from the sample plane can then be reconstructed by using the three phase demodulation technique from Equation 22. It should be noted that the modulation contrast, referred to as m in Equation 21, influences the measured brightness of the section. This value is known to vary between samples due to scattering effects and sample inhomogeneity, effectively making SIM a qualitative imaging technique [73]. However, because RLD uses the ratio of two delayed images from the same sample, where the second image intensity is essentially scaled by a multiplicative factor, we assume the modulation contrast remains relatively constant and cancels out of the lifetime calculation if there is good signal level in both images. To calculate lifetimes using SI-FLIM, a sectioned SIM image was taken at each gate and then used in Equation 3 to create a lifetime image. Each SIM image requires three modulated and phase shifted images to form a sectioned imaged for a minimum of six images when using two gates. Depending on sample quality, the number of images may need to be increased so that noise can be reduced via averaging. This averaging can significantly increase the

acquisition time. Preliminary imaging in tissue has shown that between 27 and 48 images per gate are needed. The minimum time for a single SI-FLIM gate is 5.5 seconds with a total SI-FLIM acquisition time of approximately 11 seconds for two gates. Although these times would be too slow for *in vivo* clinical applications, *in vivo* experiments using tissue immobilization mechanisms can provide a proof of concept system. Further improvements in hardware and processing can help reduce acquisition times to clinically relevant levels.

3.2.3 Method of validation

To validate that SI-FLIM can generate accurate lifetime images, the results were compared with the standard widefield RLD FLIM method. Both SI-FLIM and FLIM were co-validated by using three fluorophores with known fluorescence spectra and lifetime values (NADH, FAD, and POPOP). NADH and FAD were chosen because of their known importance as fluorescent biochemical markers of oral cancer progression [69, 74]. POPOP was chosen for its spectral similarities to collagen, another important and clinically relevant fluorescent biomarker [22]. In a homogenous solution, the lifetimes of NADH in water, FAD in water, and POPOP in ethanol are 0.3-0.5 ns, 2-3 ns, and 1.2-1.5 ns, respectively [22, 75, 76]. These were tested separately in homogenous solutions contained in 400 μm diameter quartz capillary tubes (CV4055, Vitrocom). After it was shown that SI-FLIM produced valid lifetime results, the method was tested on layered phantoms. The phantoms were made by stacking 50 μm inner diameter, 80 μm outer diameter, quartz capillary tubes (CV0508, Vitrocom). This thickness was chosen to represent 3-6 cell layers and show that our method is viable in the oral

epithelium, where it is desirable to axially isolate the fluorescence contributions of NADH and FAD in the epithelium from the submucosal collagen fluorescence (substituted by POPOP in these phantoms). The system was then tested on fixed hamster oral epithelium ex vivo from a previous study.

3.3 Results and discussion

3.3.1 SI-FLIM system characterization

The SI-FLIM system was validated in multiple steps with both the FLIM and SIM components being validated independently. After both the components were tested, the system's capability to measure the fluorescence lifetime with optical sectioning was evaluated. The lateral resolution of the system was tested using a line spread function and a Ronchi ruling. Taking the derivative of a "knife-edge" region, and measuring the FWHM yields a good approximation of the system lateral resolution [77]. The FOV was also measured using a Ronchi ruling. The axial response, or sectioning strength of the system, was measured by imaging a fluorescent layer of highlighter marker ink with ~15 μm thickness, verified by a confocal microscope with known axial resolution, 3-5 μm, as it was translated axially through the focus of the system. The average intensity of several pixels within individual SIM images was then plotted and fitted to a Gaussian distribution to approximate the FWHM of the axial response. The theoretical lateral resolution is calculated by taking the spatial Nyquist sampling rate of the camera pixels (2-3 pixels) that are imaged into the sample plane. The theoretical axial response is calculated by evaluating the optical transfer function for the frequency of the grid pattern being used to modulate the illumination source [46]. The theoretical field of view is

simply the sensor size imaged into the sample plane. Both the measured and theoretical values for field of view, lateral resolution, and axial response are shown in Table 2. Figure 10 shows the respective plots of the lateral resolution and the axial response with Gaussian estimations fitted to them.

Table 2 - Field of view, lateral resolution, and axial response (theoretical and measured)

	Theoretical (μm)	Measured (mean/st.dev 5 samples) (μm)
FOV	900	902
Lateral resolution	1.86-2.79	2.02/0.14
Axial response	32.12	35.11

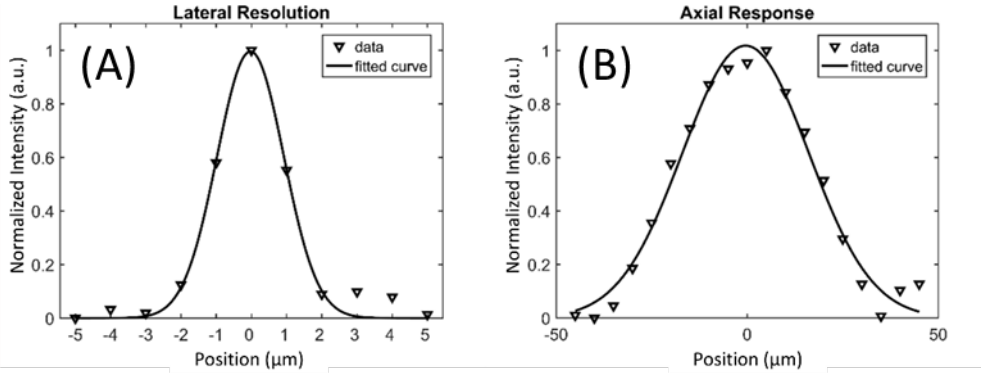

Figure 10 - (A) Lateral resolution plot from "knife-edge" Ronchi ruling with Gaussian fit. (B) Axial response plot generated by translating a fluorescent planar sample through the focus and plotting SIM image pixel intensity with a Gaussian fit.

3.3.2 Fluorescent standard validation

SI-FLIM images were compared to standard widefield FLIM images that were acquired using the same system by switching all of the DMD mirrors to the on position. The lifetime values as observed in literature and the average lifetime values as measured by widefield FLIM and SI-FLIM are listed in Table 3. Figure 11 shows representative images of each fluorophore for both FLIM and SI-FLIM where each image is taken from a 5 image set. The mean and standard deviation across each of the images in Figure 11 is shown as an overlay. The measurements for Table 3 are taken as the average and standard error of the mean lifetime values over the FOV for five images of the same sample. The capillary tubes in Figure 11 appear to be different sizes, however, this is a result of optical sectioning. Only the portion seen in the SI-FLIM sections is in focus. The widefield FLIM tubes that appear larger have more measured fluorescence from the out-of-focus planes. Because these tubes contain homogenous solutions, the out-of-focus or background fluorescence does not significantly alter the measured lifetime. For validation purposes, our reported values consist of the mean of the means for five measurements and the standard error of the mean. This data helps show that the system can make repeatable and reliable fluorescence lifetime measurements. This is shown by the small standard errors, signifying our imaging system was able to maintain very good accuracy when repeating measurements. The variability within a homogenous fluorophore sample, such as the one shown in Figure 11, is low at acceptable signal levels. The standard deviations for widefield FLIM images ranges from 0.01 to 0.1 ns and 0.01-0.2 for SI-FLIM images. This is fairly typical and is controlled mainly by the

gain being used on the ICCD and the gate width to life time ratio, but also by the contrast of the grid pattern in the sample for SI-FLIM. The noise in SI-FLIM is generally larger and is an inherent property of SIM when compared to widefield imaging. Using the average of the standard deviation values above, 0.05 for widefield FLIM and 0.1 for SI-FLIM, we define our temporal resolution to be +/– one standard deviation, thus giving 0.1 ns and 0.2 ns, respectively.

Table 3 - Widefield FLIM and SI-FLIM lifetimes in quartz capillary tubes (theoretical and measured means and standard error values for 5 samples)

		FLIM	SI-FLIM
	Literature (ns)	Measured (mean/std. error 5 samples) (ns)	
NADH	0.4-0.5	0.50/0.001	0.50/0.004
FAD	2-3	2.46/0.004	2.52/0.011
POPOP	1.2-1.4	1.43/0.004	1.39/0.013

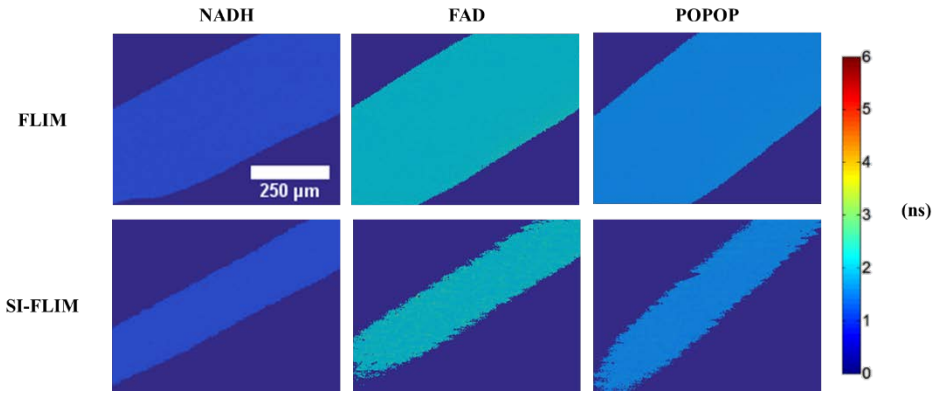

Figure 11 - FLIM and SI-FLIM image comparison, color bar in nanoseconds. The capillary tubes in the SI-FLIM images appear to be smaller; however, this is a result of optical sectioning rejecting the out of focus blur that contributes to a larger perceived size in the widefield FLIM images. Only the portion of the tube seen in the SI-FLIM images is actually in focus.

3.3.3 Stacked two layer fluorescent model

Two layer phantoms were used to demonstrate that SI-FLIM can measure the lifetimes of spectrally and spatially overlapping fluorophores that are separated along the axial dimension. Phantoms were created by stacking 50 µm diameter capillary tubes to produce two layers. The top layer tube was filled with either NADH or FAD to simulate the biochemical makeup of oral epithelium, and a bottom layer tube was filled with POPOP to approximate the spectral properties of the collagen-containing lamina propria. A second empty capillary tube in the bottom layer used as a support to keep the planes of the top and bottom tubes parallel. The tubes were arranged in a cross pattern so that each layer was evenly supported and parallel with the imaging plane.

Figure 12 shows a 3D representation of the phantom construction. The inner diameter of the tubes is 50 µm and the outer diameter is 80 µm to ensure that the center-to-center spacing of the tubes in the axial imaging dimension is ~80 µm.

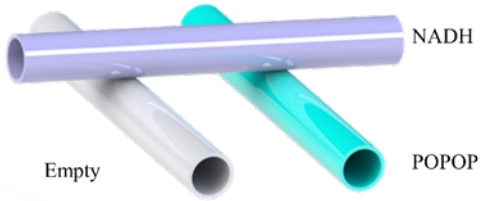

Figure 12 -Schematic of the stacked capillary model. The top purple tube represents NADH/FAD and the bottom teal tube represents POPOP.

The phantoms were tested by focusing on the center of the top capillary tube which contained either NADH or FAD. The stack was imaged with both widefield FLIM and SI-FLIM. All sectioned images were compared against non-sectioned FLIM to show that the stacked capillary tube phantoms reduce the measurement accuracy considerably if no sectioning is used. To quantitatively compare sectioning versus non-sectioning, the region of tube overlap where FAD/NADH are being imaged over the top of POPOP is compared against the areas of the image where there is no overlap. Table 4 summarizes the values measured and includes measurements of the average lifetime of NADH, FAD, and POPOP in single layer phantoms as well as the average lifetime measurements for NADH, FAD, and POPOP in the multi layered phantoms. The single layer measurements are referring to both the literature values and the measurements in Figure 13 where the tubes do not overlap, whereas the double layer measurements refer to the areas of overlap. The five measurements used in computing the mean and standard error are five repeated measurements of the same sample. Figure 13 shows both top down views of the optical phantoms focused on the center of the top capillary tubes. The lifetime data summary for Figure 13 is shown in Table 5 and the percent error summary is shown in Table 4. Equation 23 defines the percent error term used in Table 4.

Equation 22

$$PE = 100 * abs(No\ overlap\ ROI - Overlap\ ROI)/(No\ overlap\ ROI)$$

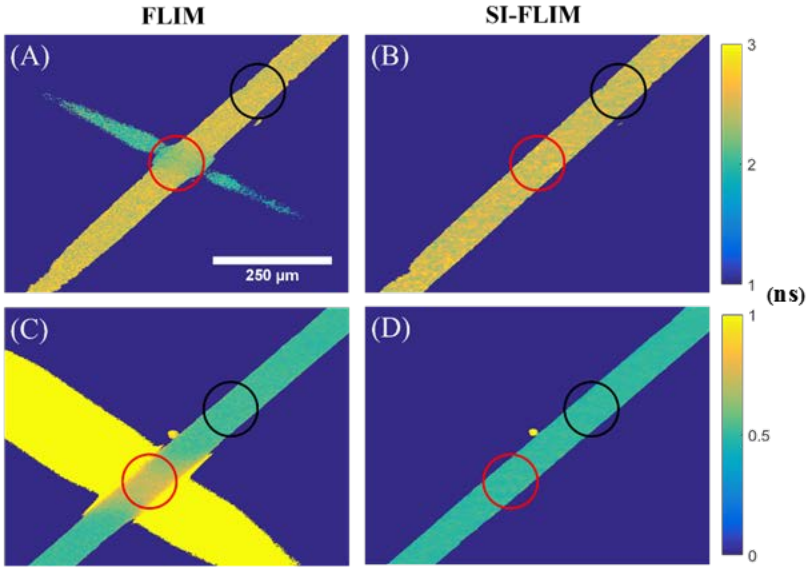

Figure 13 - Top down view of optical phantoms with focus positioned at the middle of the top capillary tube. Top row: FAD overlaid on top of POPOP imaged with (A) widefield FLIM and (B) SI-FLIM. POPOP is teal in A and B while FAD is orange-yellow. Bottom row: NADH overlaid on top of POPOP imaged with (C) widefield FLIM and (D) SI-FLIM. POPOP is yellow for C and D while NADH is teal. The color bar for A and B is adjacent to B while the color bar for C and D is adjacent to D. Both color bars are in nanoseconds. Red circles indicate the region of capillary tube overlap that is measured while black circles represent the area of the capillary tubes without overlap that is measured.

Table 4 - Comparison of widefield FLIM and SI-FLIM measurements from overlaid quartz capillary tubes containing NADH or FAD in the foreground and POPOP in the background

		Overlapping section (red circle)		Non overlapping section (black circle)	
		FLIM	SI-FLIM	FLIM	SI-FLIM
	Literature (ns)	Measured (mean/std. error 5 samples) (ns)			
NADH POPOP	0.4-0.5 1.2-1.4	0.74/0.004	0.50/0.005	0.53/0.004	0.50/0.004
FAD POPOP	2-3 1.2-1.4	2.39/0.025	2.50/0.010	2.49/0.017	2.48/0.013

Table 5 - Percent Error between expected lifetime values with no overlapping fluorophore intensities and lifetime values with overlapping fluorophore intensities

	FLIM	SI-FLIM
	Percent Error	
NADH / POPOP	38.8	0.64
FAD / POPOP	4.22	0.71

Because the lifetime of collagen, ranging from 3 ns or greater, is generally longer than that of either NADH or FAD, we expect SI-FLIM to create a net decrease on the measured lifetimes of NADH and FAD in the epithelium in comparison to widefield FLIM.[78] However, because POPOP's lifetime is between NADH's and FAD's lifetimes, we expect the lifetime for the overlapping section of NADH and POPOP to be > 0.5 ns and the overlapping region of FAD and POPOP < 2.5 ns. Figure 13 shows the effects of these overlapping fluorophores. The red circles in the figure indicate the region of overlap between the POPOP capillary tubes on the bottom and the NADH or FAD capillary tubes on the top. The black circles indicate a region with no overlap and should consist of only a homogenous fluorescence signal. The lifetimes from each region, black and red, were averaged and compared to one another. The percent error for widefield FLIM images in Table 5 shows that the red circles had a significant difference from the expected lifetime values obtained from the black circles. When looking at the SI-FLIM images, there was very little error between the lifetimes within the black and red circled regions, thus indicating that the method is successfully rejecting the out of focus light and minimizing effects on lifetime.

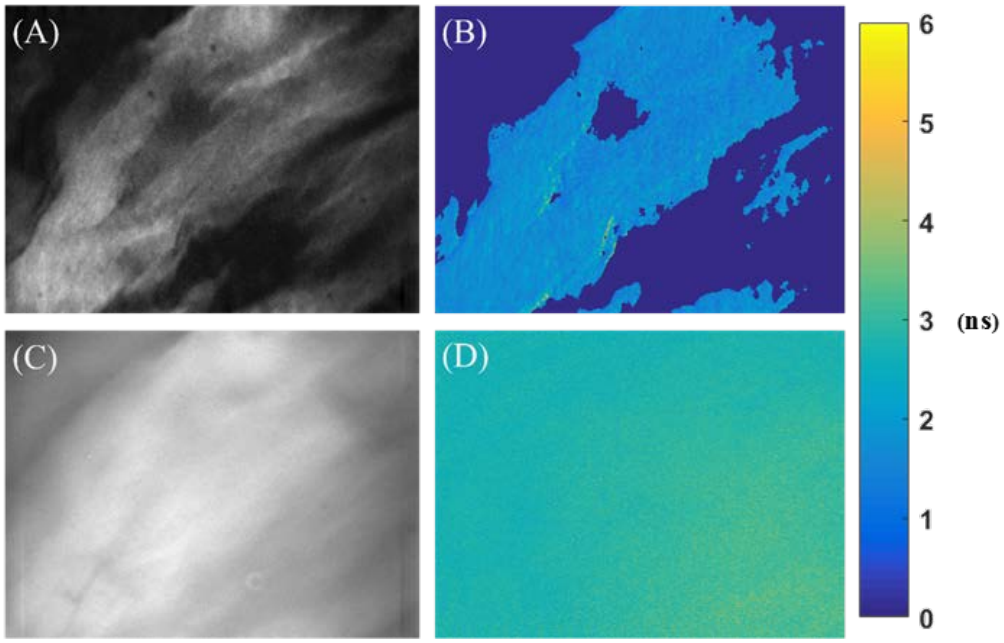

Figure 14 - Optical images of 450 nm spectral channel (targeting NADH) in preserved ex vivo hamster cheek pouch oral epithelium. (A) Sectioned image used as the first gate for the lifetime image in B. (B) SI-FLIM map of hamster cheek pouch. (C) Widefield image used as the first gate for the lifetime image in D. (D) Widefield FLIM map of hamster cheek pouch. As expected, the lifetime for the sectioned map is less than the widefield map indicating removal of submucosa collagen fluorescence.

3.3.4 Ex vivo tissue validation

Ex vivo hamster check pouch mucosa preserved in formalin was imaged to show the efficacy of the method in tissue. *Ex vivo* imaging was performed to show that SI-FLIM can mitigate the effects of collagen in the lamina propria on the measured lifetime of NADH and, to a lesser extent, FAD in the oral epithelium. As predicted, the average lifetime for the NADH channel in the hamster cheek decreased when sectioning was used, which is attributed to the rejection of the collagen signal. It should be noted that

the emission filter for these lifetime measurements was changed to a filter with the same 450 nm center wavelength but a broader 65 nm bandwidth (HQ450/65M, Chroma). This was done to increase our signal level while still maintaining a similar spectral band. A series of five SI-FLIM and widefield FLIM images were taken at five different locations and compared to verify that the collagen rejection effect can be observed at many different locations. Figure 14 shows the effects of sectioning on the *ex vivo* hamster cheek pouch oral epithelium for the NADH spectral window. A non-parametric Wilcoxon rank sum test was used to verify that the SI-FLIM images and widefield FLIM images are from statistically different ($p < 0.05$) populations. For each measurement, FLIM and SI-FLIM, five different locations were imaged. The mean lifetime/standard error for FLIM was 2.76/0.05 ns and for SI-FLIM it was 1.70/0.13 ns. Although we did not validate our system in a scattering phantom, results from our *ex vivo* experiments indicate that SI-FLIM should provide meaningful information in scattering samples such as tissue.

At 355 nm excitation, collagen has a notable overlap in its emission spectra with NADH. This can potentially confound and reduce one's ability to accurately resolve the fluorescence lifetime of NADH.[70, 79] Optical sectioning techniques that can remove the influence of the spectral overlap via spatial separation would theoretically be able to improve the accuracy of the NADH lifetime measurements. Both Figure 14 and Table 5 show that SI-FLIM has the effect of lowering the measured lifetime in the NADH (450 nm) channel. This was the predicted effect optical sectioning was expected to have due to NADH possessing a much shorter lifetime than that of collagen.[21, 22] This theory is

also supported by the data shown in Figure 13, Table 3, and Table 4 where the effects of NADH overlaid on POPOP, a collagen substitute, are minimized and it is shown that the NADH lifetime is completely recovered without any influence from POPOP. This phenomenon can potentially be utilized to enhance the sensitivity of in vivo lifetime imaging systems for cancer diagnostics where the fluorescence signal from the collagen fluorescence may dominate the NADH channel and reduce the ability to accurately measure the change in NADH lifetime.[21] Our technique has the potential to enable resolution of relatively small changes in NADH lifetimes in epithelial tissue by removing the effects of collagen on NADH. This increased ability to detect more minute changes in NADH lifetimes could lead to the ability to detect precancerous tissue earlier and may also allow to one to differentiate between benign and malignant tissue.

In addition to collagen, keratinized epithelial tissue presents a similar challenge.[80] Keratin has a fairly large spectral overlap with NADH fluorescence lifetime similar to that of collagen, which can also confound the NADH measurement and reduce accuracy.[79, 81] Unlike collagen, the keratinized epithelium is superficial to the NADH containing epithelium. By using SI-FLIM, it may also be possible to image a section of the epithelial tissue that rejects the fluorescence signal from the keratinized epithelium superficial to it as well as the collagen containing connective tissue below it, leaving only fluorescence from the epithelium that contains NADH. This is supported by the observation of background rejection using structured illumination and by considering the symmetrical shape of the axial response function. Complications could arise in keratinized epithelium if the grid pattern cannot be resolved underneath it.

3.4 Summary

We have shown that SI-FLIM can produce accurate lifetime measurements in homogenous samples as well as in multi-layered phantoms where each layer has spectrally overlapping fluorophores. In addition to demonstrating SI-FLIM's ability to accurately reconstruct lifetimes in three dimensions, we demonstrated that it greatly reduced the effects of the collagen/POPOP that confounds the measurements of NADH and FAD's lifetimes in oral epithelium. Being able to measure these fluorophores independently is of great interest to those researching optical oral cancer detection. NADH and FAD are important metabolic cofactors that exist in either a protein bound state or free state where their fluorescence lifetime depends on the state.[36, 40] Tissue undergoing carcinogenesis has a marked change in the states of both FAD and NADH due to changes in cellular metabolism.[69] We believe that measuring these lifetimes without the influence of the collagen signal will potentially give the ability to create a significantly larger contrast between precancerous and benign or normal tissue. The following work will discuss the testing of our SI-FLIM system on the hamster cheek pouch model of oral carcinogenesis *in vivo.*

CHAPTER IV

ENHANCED EARLY DETECTION OF ORAL CARCINOMA BY STRUCTURED ILLUMINATION FLUORESCENCE LIFETIME IMAGING MICROSCOPY

4.1 Introduction

We have thoroughly discussed oral squamous cell carcinoma, its effects on people, the current methods of diagnosis, and novel methods of diagnosis in the preceding sections within this paper. Although the reader may now be familiar with these concepts, the following introductory text will briefly recapitulate the overview of OSCC, its current diagnostic methods, and the new method employed in this thesis.

OSCC is characterized by poor prognosis and a low survival rate.[10] As with most cancers, a variety of conditions, both environmental and genetic, can lead to its development. Some of the main risk factors associated with the development of OSCC in humans are the usage of tobacco and alcohol, especially in conjunction, the human papilloma virus (HPV), as well as a genetic predisposition to developing the disease.[10, 12] Oral cancer is of particular concern because of its propensity to either be fatal or cause morbidity in patients who survive diagnoses and treatment.[15] The current standard of care to screen for oral cancer is via examination of the oral cavity by a trained clinician with subsequent histopathological analysis. The examination is conducted either visually, by palpation, or both.

If a suspicious area is identified, a biopsy is taken for histopathological diagnosis.[16] As mentioned earlier, a major problem with this method is that there is an inherent delay between the identification of a potentially malignant/pre-malignant lesion and its accurate histopathological diagnoses. Additionally, many indications of oral disease are often diffuse and multi-focal, which makes screening of the whole oral cavity even more challenging. A potentially better alternative would be to be able to accurately and quickly diagnose malignant and premalignant lesions within the mouth with a non-contact optical imaging method. This would not only allow for a clinician to make more accurate margins for biopsy, but also has the potential to replace many investigational biopsies.

One of the most promising optical imaging modalities is fluorescence lifetime imaging microscopy. This method allows us to measure the duration of fluorescence emitted from fluorophores when stimulated with a pulse of light. The key feature of fluorescence that allows FLIM to be used a diagnostic tool is that the lifetime of fluorophores is characteristic and can change depending on the local environment of that fluorophore, e.g. binding to a protein or pH changes. FLIM, for the purposes of OSCC detection, ideally aims to measure the change in the fluorescence lifetime of the metabolic cofactors NADH and FAD with the onset of carcinogenesis. NADH and FAD are molecules that aid in redox reactions during cellular metabolism.[37] It is well documented that carcinogenesis creates a fundamental shift from oxidative phosphorylation to glycolysis. This results in a variety of factors that affect the lifetime of NADH and FAD.[82] In general, the onset of carcinogenesis produces a decrease in

NADH lifetime and an increase in FAD lifetime.[38] However, external factors prevent FLIM from being readily used in NADH and FAD lifetime imaging within the oral epithelium. Background fluorescence from out of focus fluorophores interferes with standard measurement techniques like the RLD method used in this work. The main source of this out of focus fluorescence is collagen and is caused by all three fluorophores, NADH, FAD, and collagen, possessing fluorescence with UV excitation.[79] The largest concern is that there is significant spectral overlap between the NADH emission and the collagen emission that exists within the same imaging pixel. To address this, we utilized the morphology of the tissue. Because collagen exists mainly in the submucosa deep to the epithelium and NADH exists mainly in the epithelium, optical sectioning could be used to preferentially image the NADH containing epithelium while rejecting the collagen in the submucosa.

To this end, we have pursued the development of a fluorescence lifetime imaging microscope that utilizes optical sectioning via structured illumination.
SI-FLIM has been shown to provide depth dependent fluorescence lifetime information.[18] The test apparatus used in (*Hinsdale et al. 2017)* consisted of two capillary tubes stacked on top of one another with 80 μm between centers. The top capillary tube contained either NADH or FAD and the bottom tube contained POPOP, a fluorescent collagen substitute. It has shown that overlapping regions of POPOP and NADH possessed an average lifetime between the two when imaged with standard widefield FLIM. However, when using SI-FLIM, the lifetime of the focal plane containing NADH was fully recovered as if it was imaged as a single homogenous

sample using widefield FLIM. To extend this method to a clinical diagnostic tool, pre-clinical animal studies needed to be carried out. Golden Syrian hamsters (*Cricetus auratus*) have been used before as model for the optical detection of OSCC using FLIM.[83] The following text reviews a 12 week pre-clinical animal study for the purpose of evaluating SI-FLIM as a method of enhancing the early detection of OSCC.

4.2 Materials and Methods

4.2.1 Tissue preparation

The Syrian golden hamster (Cricetus auratus) model for OSCC using 7, 12-dimethlybenzene[a]anthracene (DMBA) was used because its application to the hamster model of sequential oral oncogenesis closely resembles the formation of oral cancer in humans.[10, 83] The animal use protocol (AUP) was approved by the Texas A&M University Institutional Animal Care and Use Committee (IACUC). Twelve male hamsters were acquired between five and six weeks in age. They were allowed to acclimate to their environment for a total of one week after their arrival. The hamsters were divided into two groups, a control group and treatment group. The control group consisted of three hamsters, and the treatment group consisted of nine. The treatment group was further subdivided into three groups that represented six-week, nine-week, and twelve-week treatments with DMBA. The treatment group received an application of DMBA as the carcinogenic factor in mineral oil (as a carrier) on their right cheek pouch and pure mineral oil on the left cheek pouch. The control group exclusively received treatments with pure mineral oil. Treatments were applied to the hamsters under 3-4% isoflurane anesthesia. The mineral oil solutions were administered via No. 5 paint

brushes. The treatment process was carried out on the hamsters until their imaging time point, up until a maximum of twelve weeks. Throughout each week, the hamsters were administered three evenly spaced treatments. Beginning at the sixth week of the treatments, the three control hamsters were imaged and euthanized along with the sixth-week hamsters from the treatment group. Following this, the ninth-week group and twelfth-week group were imaged and euthanized accordingly. The cheek pouch tissues were harvested post-mortem for histopathological processing.

4.2.2 Imaging protocol

Immediately prior to imaging, each hamster was anesthetized with a 10% w/v urethane (Sigma-Aldrich) solution in de-ionized water. After the animals became fully sedated, their cheek pouches were mounted into a custom-made brace designed to immobilize and flatten the tissue, yet allow blood flow to the cheek. This process was performed on the treated and the contralateral, mineral oil only, sides separately. The exposed cheek area available for imaging, approximately 16 mm x 16 mm, was subdivided into three imaging lines that were equally spaced along one of the 16 mm dimensions to assist with histology registration. These three lines were further divided into four equally spaced quadrants, resulting in a defined 4x3 grid with 12 defined imaging regions, see Figure 15. Any regions of the epithelium that appeared visually distinct to the eye were imaged separately after the first twelve images.

The imaging consisted of capturing two time gated intensity images. The first gate was initiated at the peak of the intensity decay with an exposure time of 1 ns. The second gate was delayed by 1 ns and possessed the same exposure time. Capturing a

standard widefield FLIM image requires a minimum of two gated images per lifetime.[71] However, to perform SIM a minimum of six gated images, three modulated phase shifted images per time delay, are required.[18] Three spectral emission bands were imaged: 390nm +/- 20nm, 450nm +/- 20nm, and 550 nm +/- 16nm. These three bands correspond to the primary spectral band of the emission of the three fluorescent markers of carcinogenesis: collagen, NADH, and FAD, respectively. Figure 15 shows a diagram of the imaging setup and how it was used on the hamster cheek. For future context, when referring to the spectral channel being imaged, we will refer to them by the expected dominant fluorophore of that specific bandwidth. To remain consistent, the imaging order of spectral bands was maintained as 1) NADH, 2) FAD, and 3) collagen. Each channel was imaged with WF-FLIM. Only the NADH channel was measured with SI-FLIM first then WF-FLIM second. Moving forward, the NADH channel as measured by SI-FLIM will be labeled as SI-NADH, and the NADH channel as measured by WF-FLIM will be labeled as WF-NADH.

4.2.3 Image processing

The FLIM data was obtained in two formats: raw intensity images for each widefield gate and raw modulated phased shifted images for each SIM gate. The raw structured illumination images first were processed using the standard three phase demodulation technique to create sectioned images for each gate delay.[45] See Equation 22 for reference. A widefield image can be calculated by averaging the three phase shifted gates and was used to create spatial masks for later analyses. These sectioned images, along with their widefield counterparts, were used to calculate

fluorescence lifetime maps for each spectral band using the rapid lifetime determination (RLD) method shown in Equation 3.

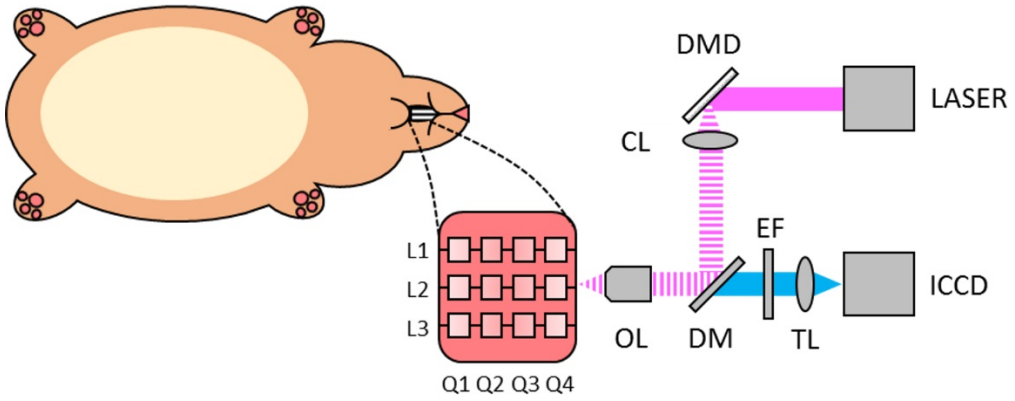

Figure 15 - Diagram of experimental setup for imaging oral carcinoma development in hamster cheek pouch. A hamster is anesthetized and its cheek pouch is everted to give ~16mmx16mm imaging area. Three lines were designated by L1,2,3 and four quadrants by Q1,2,3,4. A conceptual drawing of the SI-FLIM devices is shown on the right. OL (objective lens), DM (dichroic mirror), EF (emission filter), TL (tube lens), ICCD (intensified CCD), CL (collimation lens), DMD (digital micromirror device), Laser (355 nm, 1.5 ns, pulse laser). Focusing was achieved via a translation stage, not shown.

Before computing the fluorescence lifetime images using Equation 3, image masks were generated so that only pixels of sufficient quality were included in our final lifetime analysis. The first mask was based on gray level thresholding to distinguish in focus from out of focus regions using the sectioned intensity images. The other mask was based on signal to noise ratio (SNR) and utilized a sliding SNR filter to calculate local SNR maps. Here the signal is defined as the mean of a sliding 7x7 kernel and the noise is

the standard deviation of the background. The second gate was used to calculate the SNR maps to ensure that the lowest intensity acted as our cutoff limit. The first set of SNR masks were generated using the standard widefield intensity image and the reconstructed widefield intensity image. The SNR cutoff for each was set to >20 dB for the widefield images, a typical value for fluorescence lifetime imaging.[84] The third SNR mask was made using the second gate of the sectioned images. Structured illumination is known to have relatively reduced SNR, and because of this, we lowered our SNR criteria for the sectioned image to > 13 dB.[84, 85] Even though this value is lower than desirable, and future systems would take great care to enhance the SNR, it should still be sufficient. The lifetime images were then calculated using Equation 3 and spatially averaged using a smoothing mean filter. A histogram was then made of each lifetime image and the median value was extracted for statistical analysis. The median values are useful for visualizing trends within an animal, but lack robustness when it comes to cross animal comparison. This could be due in part to physiological conditions that developed in individual hamsters over the course of treatment unrelated to carcinogenesis. To normalize for this, the median lifetime values from the contralateral, mineral oil only, images were averaged on a per animal basis and subtracted from the images on their paired treatment sides. In this way, a lifetime delta was created between the treatment and contralateral side and helped reduce inter-subject variability by providing a lifetime shift from a normal baseline for every animal. The contralateral normalization was done for both WF-NADH and SI-NADH independently of one another.

4.2.4 Statistical analysis

A statistical analysis was carried out on the normalized median lifetime values that were extracted from each image. To perform a comparison of the values, they were put into three main classes: normal, mild dysplasia, and carcinoma. The three classes contained 26, 17, and 9 regions of interest (ROIs), respectively. The classes were based on histopathological diagnoses provided by an experienced clinical pathologist. Each class (normal, mild dysplasia, and carcinoma) spans several hamsters as well as contains multiple ROIs from the same animal. As mentioned in the previous section, a normalization procedure was done to reduce the effects of inter-subject variability. For further analysis, it is relevant to note that some samples' ROIs were in close proximity to one another and used the same histopathological classification, but none of them were physically overlapping. This allows us to treat each ROI as an independent data point. To start, each class was tested for normality and followed by two one-way ANOVAs. The two one-way ANOVAs were run to compare the separation of the normal, mild dysplasia, and carcinoma classes for each detection method. Due to unequal variances, the Brown-Forsythe method was used for the initial ANOVA testing.[86] After significance was found, a post-hoc analysis was conducted using the Games-Howell correction for unequal variance and sample size.[87] We then generated ROC curves using a proper binormal model in the task for distinguishing mild dysplasia from normal tissue.[88] This was done to compare and contrast SI-NADH against WF-NADH with the ultimate goal of showing that SI-FLIM has the potential to be a better indicator of the early stages of pre-malignancy when compared to WF-FLIM.

4.3 Results

4.3.1 The effects of SI-FLIM on the measurement of the NADH channel

Our initial hypothesis was that SI-FLIM would be able to better reconstruct the true NADH fluorescence when compared to widefield FLIM. As discussed earlier, the hypothesized reason behind this is a rejection of the background fluorescence emanating from the collagen channel that is spectrally overlapped with the foreground NADH channel. Figure 16 illustrates the effects of SI-FLIM on the measurement of the NADH channel quite clearly. Note the data compared here is before normalization. Figure 16 (A) and (B) represent the SI-NADH and WF-NADH lifetime values for a normal control hamster. Figure 16 (C) visually compares the distributions of the WF-NADH and SI-NADH channels for a subset of the control hamsters, where the subset was made by selecting every other data point in the set. To statistically compare SI-NADH against WF-NADH, a paired t-test was performed on all of the control hamsters and provided a significant difference between the two groups ($p<0.05$).

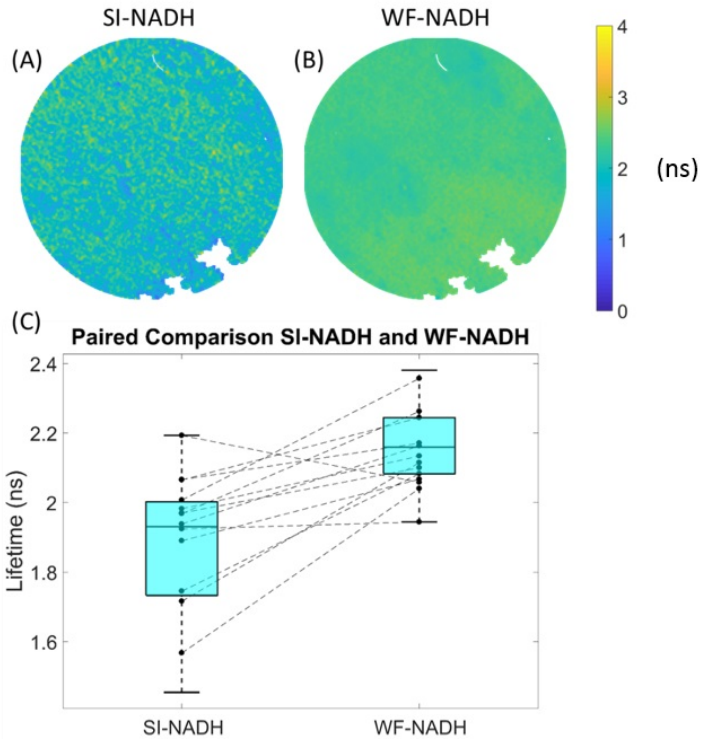

Figure 16 - (A) SI-NADH image and (B) WF-NADH image of an example control hamster cheek pouch. (C) Paired relationship plot between SI-NADH and WF-NADH for control animals. SI-NADH on the left is shown to be generally lower than WF-NADH on the right. A paired t-test revealed that the observed relationship in the graph is statistically significant.

4.3.2 Typical data of SI-FLIM

Before exploring the results, it is helpful to glimpse a snapshot of a typical SI-FLIM data set. For all regions of interest, a typical SI-FLIM data set consists of a series of time gated images from both structured illumination, SI-FLIM, and WF-FLIM. These images are then used to compute the lifetime maps that accompany the gated images in Figure 17. However, only the NADH channel is imaged with both modalities, while FAD and collagen are only imaged with WF-FLIM. For this reason, we will focus on

presenting the differences between the SI-NADH and WF-NADH channels. As discussed earlier, all lifetime values displayed in Figure 17 are the change in lifetime from the contralateral lifetime values of each channel. The lifetime images appear circularly cropped to the smallest dimension of the detector plane due to its unequal aspect ratio ~ (4:3).

We can see that the lifetime delta values become lower relative to the normal cases for both imaging modalities with the progression of carcinogenesis. A key characteristic driving this is that the fundamental metabolic processes of the epithelial cells shifts from an oxidative metabolic state to a glycolytic metabolic state that results in a shortening of the NADH lifetime.[37] So, on average, the lifetime delta should become more negative as cases become more severe.

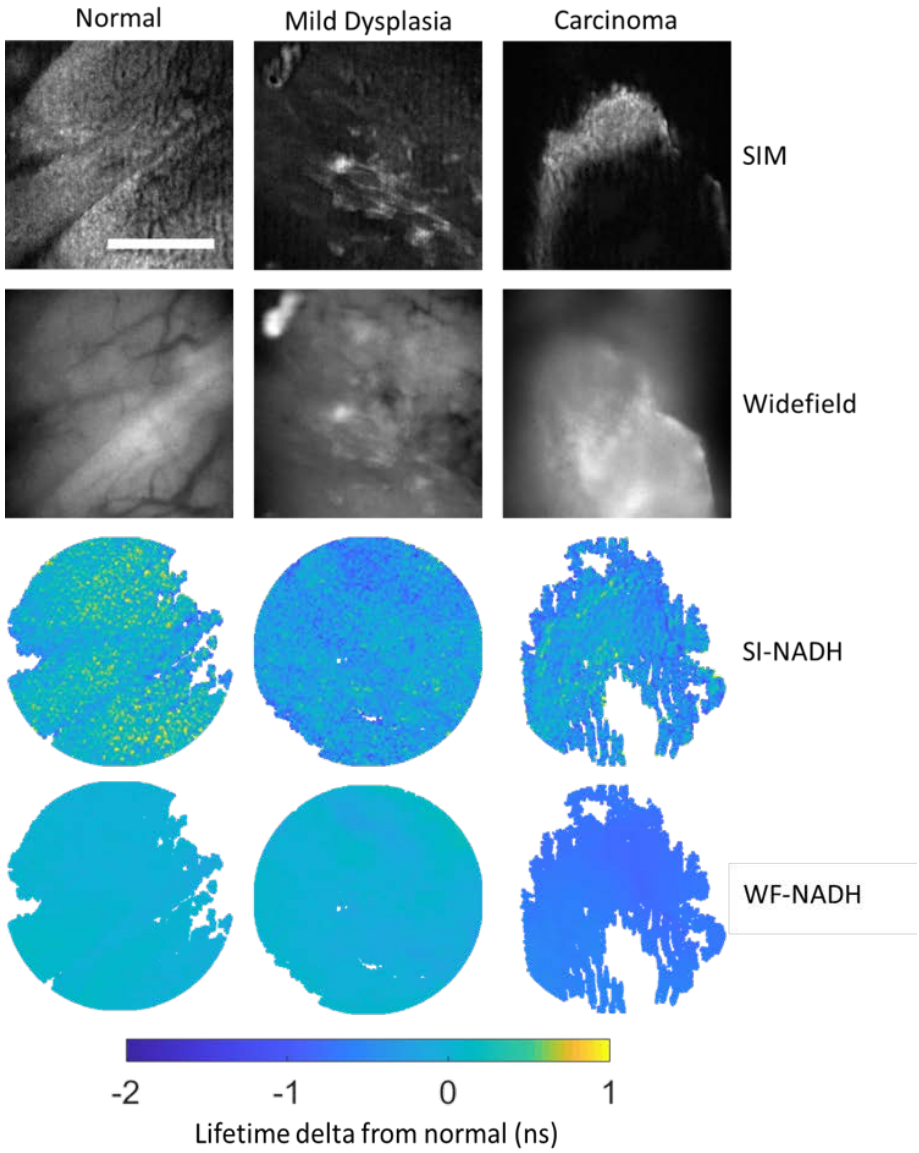

Figure 17 - Example set of images used for analysis. Includes three cases (L-R): Normal, Mild Dysplasia, and Carcinoma. Includes four image subtypes (top-bottom): SIM intensity image, Widefield intensity image, SI-NADH, WF-NADH. Scale bar is 220 µm in length.

4.3.3 Statistical comparisons

Brown-Forsythe ANOVA tests performed on the normal, mild dysplasia, and carcinoma classes for the WF-NADH channel yielded statistically significant results ($p = 0.007$). Similarly, the Brown-Forsythe test for the SI-NADH channel yielded a p-value = 0.001. Consequently, post-hoc tests utilizing the Games-Howell correction were performed. Note that the post-hoc tests were only comparing the classes within a specific channel, i.e. WF-NADH (mild dysplasia = carcinoma, mild dysplasia = normal, normal = carcinoma).

Table 6 - Summary of statistics for the SI-NADH and WF-NADH lifetime channels. P values are shown where significance indicates a rejection of the null hypothesis stated in the left column. Mean lifetime values and standard deviation are displayed based on the verification of approximate normality.

Null hypothesis	SI-NADH	WF-NADH
Class A = Class B	p-values	
Mild Dysplasia = Normal	0.001	0.897
Mild Dysplasia = Carcinoma	0.929	0.027
Carcinoma = Normal	0.022	0.034
	Mean/St.Dev Lifetime Deltas	
Normal	-0.01/0.19	0.00/0.12
Mild Dysplasia	-0.32/0.26	0.03/0.23
Carcinoma	-0.36/0.29	-0.31/0.27

From Table 6, we can see that SI-NADH may be a better indicator of mild dysplasia when compared to WF-NADH. This comes from the fact that SI-NADH possesses a statistically significant difference in lifetimes between normal and mild dysplasia, while WF-NADH does not. This is important in clinical cases where the diagnoses of pre-

malignant lesions early in the process is critical to patient health. These differences in mean lifetime delta from normal can best be visualized in trend graphs that plot the mean and standard error of each class for each channel, SI-NADH and WF-NADH. We can also see that SI-NADH cannot distinguish between mild dysplasia and carcinoma, while WF-NADH can. We can most likely attribute this to the effects of epithelial thickening during carcinogenesis.

The fluorescence lifetime measurement of NADH is usually obscured by background collagen fluorescence overshadowing it in a normally thin epithelium. Although there are detectable changes in the NADH lifetime during mild dysplasia, they are usually hidden. Structured illumination addresses this by optically sectioning away the collagen from the epithelium, allowing for the measurement of changes in the NADH lifetime. WF-NADH shows a similar drop in lifetime, but only during the more advanced stages of carcinogenesis. This behavior is clearly shown in Figure 18 (A),(B). We hypothesize that this is possibly because of the epithelial thickening and invasion into the submucosa that occurs with carcinogenesis.[89] This process both distances the collagen from the image plane in the epithelium and degrades the fluorescence as the epithelial cells invade the submucosa. Because of the morphological changes that occur and the diminishing fluorescence of collagen, the changes in the NADH lifetime are able to be viably measured with WF-NADH in the advanced stages of carcinogenesis. Our data suggest that there is a significant lifetime shift during mild dysplasia that can be measured by SI-NADH, but is only available to WF-NADH during more advanced stages. However, SI-NADH does not have a significant decrease between mild dysplasia

and carcinoma. Qualitatively, a decrease can be seen in Figure 18 (A), but the data was too variable to make any conclusions. We should also consider the small sample sizes of the classes in the two groups, WF-NADH and SI-NADH, and the variability of the carcinoma class. Additionally, this phenomenon could be unique to our system and induced by a systemic procedure. Other authors' work indicates that the lifetime should keep decreasing, but, as just mentioned, the variability in our data was too large to draw any statistically significant conclusions.[38] Regardless, Figure 18 (A),(B) succinctly shows the evolution of the lifetime differences as oral epithelial tissue progresses through the stages of carcinogenesis.

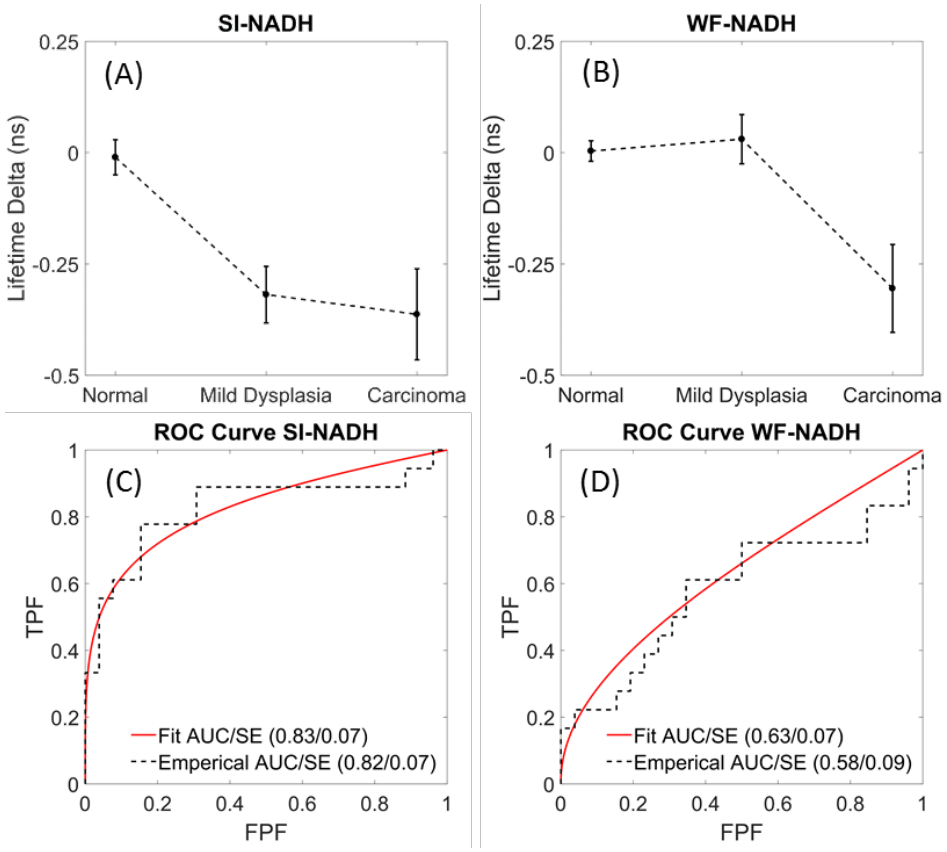

Figure 18 - Trend in lifetime deltas of the (A) SI-NADH and (B) WF-NADH channels for normal, mild dysplasia, and carcinoma. Data points are of the mean lifetime delta and error bars are +/- one standard error. Standard error was used to illustrate the relative certainty of the mean value for each class. ROC curves compare the differentiating power of (C) SI-NADH and (D) WF-NADH for cases of mild dysplasia against normal. The fitted curves were made using a proper binormal model.

To explore the use of SI-FLIM as a diagnostic test, the raw lifetime deltas can be used to generate ROC curves in the task of distinguishing between normal tissue and mild dysplasia. We reduce the complexity of this model by only considering the ROC curve between normal and mild dysplasia for a single feature at a time. This case is of particular interest because it indicates that SI-NADH may be able to better detect

malignancy in its early stages of development. The results of both curves are then compared to evaluate which one acts as a better discriminator in this limited case. Figure 18 (C),(D) directly compares the ability of SI-NADH to discriminate normal tissue from mild dysplasia against the ability of WF-NADH. The empirical ROC curves are shown plotted alongside their proper binormal fitted models. Because we assume that WF-NADH will perform worse, it should have a lower area under the ROC curve. Knowing this, we can perform a one-tailed t-test between the curves and show that the area under the ROC curve for SI-NADH is statistically larger than the area under the ROC curve for WF-NADH ($p = 0.031$).[34] Keep in mind that this was performed on a binormal fit and not a proper binormal fit to the empirical ROC data.

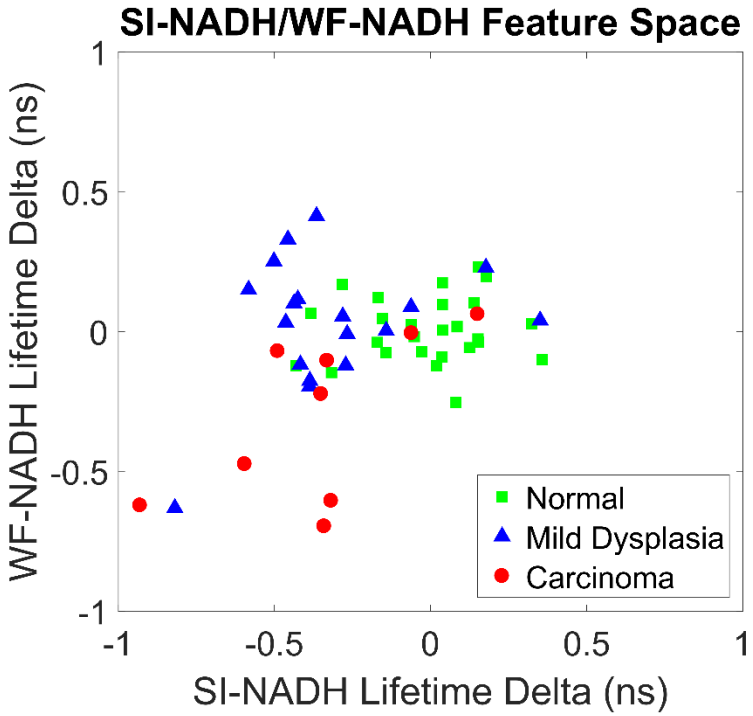

Figure 19 - Feature space comparing the relationship between SI-NADH and WF-NADH for three diagnostic cases (normal, mild dysplasia, and carcinoma). Normal resides mostly around a zero delta from itself, as expected. Mild dysplasia shows displacement preferentially along the SI-NADH axis. Carcinoma shows displacement on both axes equally.

Although SI-NADH is superior in this case, it cannot distinguish between mild dysplasia and carcinoma. Because WF-NADH can be used to distinguish between carcinoma and all other cases, one can easily extrapolate a decision tree to determine which pathology class a given image is in based on the lifetime delta for both WF-NADH and SI-NADH. To help visualize this it is useful to plot the data points in a feature space. Figure 19 shows the two dimensional feature space with SI-NADH on the lateral axis and WF-NADH on the vertical axis. Three classes, are defined in the legend: normal, mild dysplasia, and carcinoma. The class separations shown in Figure 19 are

readily visible in Figure 18, but with the added benefit of a more holistic view pertaining to interclass relations. Note that mild dysplasia shows preferential displacement along the SI-NADH axis. This means that the majority of the discrimination power is coming from SI-NADH in this case. For carcinoma, there is approximately equal displacement on both axes, yielding similar discrimination power to both SI-NADH and WF-NADH. A crucial part to note is that SI-NADH does not discriminate between carcinoma and mild dysplasia while WF-NADH does. Therefore, this results in three clusters contained within the two dimensional feature space defined by SI-NADH and WF-NADH. With further experiments, and more data, a classifier could be trained to discriminate between the three class clusters.

4.4 Discussion

SI-FLIM was first evaluated by determining its effects on the measurement of the NADH spectral channel. SI-NADH, the NADH channel as measured by SI-FLIM, exhibited the expected behavior that we hypothesized. That is that using SI-FLIM on normal tissue to measure the NADH spectral channel lowered the observed lifetime value when compared to WF-FLIM. The proposed mechanism is that structured illumination preferentially imaged the in-focus content, which is the oral epithelium in our case, and rejected the out of focus light. In epithelial tissue, the out of focus light predominately emanates from the submucosal connective tissue and is composed primarily of collagen.[80] This is evaluated quantitatively by performing a paired t-test between SI-NADH and WF-NADH for all normal regions. The results proved to be statistically significant, so we continued our analysis. Although we measured other

fluorophores with widefield FLIM, the only fluorescence channel measured with both modalities was the NADH channel. This was done to limit the amount of UV exposure and reduce photo bleaching of the sample caused by the extended time necessary to acquire SI-FLIM images.[18] Hence, our analysis focused exclusively on the efficacy of SI-NADH as a diagnostic feature against that of WF-NADH. In the future, this method could be easily extended to incorporate SI-FAD as a feature. To do this, the imaging rate would need to be increased so that there is adequate signal for structured illumination when imaging FAD. As of now, much of the signal is reduced by extended imaging and photo bleaching when evaluating NADH. An alternative would be to multiplex the imaging so that multiple spectral channels could be imaged at the same time.

Regions of interest were put into three classes: normal, mild dysplasia, and carcinoma based upon a histopathological diagnosis. These classes were then compared against one another using an ANOVA for each feature of interest, SI-NADH and WF-NADH. This showed that SI-NADH could discriminate between mild dysplasia and normal within our samples, while WF-NADH could not. At a fundamental level, this validated our hypothesis and is strong evidence that this pilot study merits a longer follow-up study with more animals. Although our analysis yielded promising results, we believe that they could have been enhanced by certain improvements to our system. To start, the measured lifetime features consisted of the median lifetime values for a given field of view of ~0.9 mm diameter. *In vivo* FLIM for diagnostic purposes is typically performed over a much larger field of view, ~2-10 mm diameter.[21, 22] This much smaller field of view could have contributed to completely missing entire diagnosed

regions. In the methods section, we defined an imaging grid that contained twelve regions, three lines with four quadrants per line, in an approximately 16 mm x 16 mm area. The position of the imaging lines relative to the histology tissue section is fairly certain; however, each quadrant occupies a 4 mm section with one 0.9 mm field of view taken in it. Another factor that influences co-registration is tissue shrinkage and damage during fixation and histopathology. Because of this, images that were directly adjacent to the diagnosed quadrant were considered to possess the same diagnosis. This could have produced regions of interest that were not co-registered with the histopathological diagnosis they were assigned. One place where this evident is in Figure 19. A handful of carcinoma diagnoses appear firmly center of the cluster of normal diagnoses. However, the uncertainty in our image placement within the histopathologic sections leaves us unable to reject them from the analysis. With better co-registration, by either increasing the field of view or increasing the imaging speed to acquire more fields of view, this would be less of an issue. The three phase SIM technique was the major limitation to our imaging speed, but new advances that only require one structured image could alleviate this problem.[90] Poor contrast of the illumination pattern in the epithelium also presented a challenge. Our experiment used an air objective, leaving the oral epithelium exposed to the environment. What appeared to be secretions from the epithelium reduced our ability to resolve the structured illumination pattern and required drying the tissue via compressed air prior to imaging. This could easily be solved in future experiments by implementing a water immersion physiology lens.

The efficacy of SI-NADH and WF-NADH in the task of discriminating between mild dysplasia and normal is shown in Figure 18. It is clear that SI-NADH is the superior discriminator in this sense, an observation which is validated by statistically comparing the two ROC curves. When not looking at a relative comparison, SI-NADH performs well but not outstanding. This manifests when looking at the slowly climbing value of TPF with increasing values of FPF. With a TPF of 0.75, the FPF is 0.24. This results in a sensitivity and specificity of 75/76%. Values closer to 85% would be more desirable. A large part of this is due to the existence of a handful of values which are considered statistical outliers by definition of being 1.5 times above or below the interquartile range of their respective class. Removing these points from the data set drastically raises the area under the ROC curve for SI-NADH while leaving WF-NADH largely untouched. For example the area under the empirical ROC curve for SI-NADH is pushed to 0.92 while WF-NADH goes to 0.69. Regardless, the small sample size, and large variances, do not give us adequate evidence to treat these values as outliers and we must therefore use the prior values for sensitivity and specificity. As a precursor to developing a machine learning classifier, WF-NADH and SI-NADH are plotted in a two dimensional feature space where the three clinical diagnoses are considered classes. Figure 19 gives an overview of the between-class separation for each diagnosis in terms of WF-NADH and SI-NADH lifetime deltas from normal. One shortcoming is that the carcinoma class is highly varied and possesses the lowest sample number. This on its own led us to not seriously consider training a classifier that could distinguish between all three classes.

CHAPTER V

CONCLUSION

In summary, we demonstrated that structured illumination could be used in epithelial tissue to image at cellular resolution and resolve multiple cell layers, that it could be combined with fluorescence lifetime imaging to accurately resolve the lifetimes of axially separated but spectrally overlapping fluorophores, and that the combination of the two modalities has the potential to be a useful discriminator between the early stages of pre-malignancy (mild dysplasia) and normal tissue. Much work needs to be done before SI-FLIM can be considered for clinical translation. Even though taking an image with the SI-FLIM system is much faster than a standard tissue biopsy with histopathological analysis, it is still relatively slow when compared to other *in vivo* cancer imaging modalities such as RCM or standard non-sectioning FLIM.[21, 91] The slow imaging speed could present problems when trying to reduce the effects of motion artifacts where true high-speed video-rate imaging would be desirable. The sensitivity and specificity of SI-NADH as a discriminator between mild dysplasia and normal tissue is 75/76%. These values are lower than desirable for clinical considerations, but also somewhat arbitrary as they are generated by picking a point on the SI-NADH ROC curve in the task of discriminating between mild dysplasia and normal tissue. Acceptable sensitivity and specificity percentages for clinical diagnostic tools tend to be above 80/80%.[92, 93] While the SI-NADH values were close, they never exceeded or met a sensitivity and specificity of >80/80% concurrently. Choosing this cutoff is further complicated by the fact that the risk factors associated with various diseases can

influence which value, sensitivity or specificity, is more important. Some diseases are better suited for test that have a very high sensitivity while sacrificing specificity, or vice versa. A more easily approachable method for initially determining how useful a diagnostic test will be in general is to look at the area under the ROC curve.[94-96] The AUC for the SI-NADH ROC curve in the task of distinguishing between mild dysplasia and normal tissue is 0.83. This falls into what is considered the good range for a discriminatory model, $0.8<AUC<0.9$. An excellent model's AUC falls in the range of $0.9<AUC<1.00$. Because of the highly controlled pre-clinical testing environment, we would ideally like to see an AUC in the excellent range. All points considered, this method has the potential to lower the time delay between the onset, the detection, and the subsequent treatment of oral squamous cell carcinomas. Future work includes refining the optical system, making it faster, and potentially incorporating a flexible fiber endoscope. The preliminary pre-clinical trial discussed in this paper has provided enough evidence to continue with another, larger, pre-clinical study after the system is improved.

REFERENCES

1. Hejmadi, M., *Introdcution to Cancer Biology*. 2010, Holstebro, Denmark: Ventus Publishing. 48.
2. Alizadeh, A.M., S. Shiri, and S. Farsinejad, *Metastasis review: from bench to bedside.* Tumor biology, 2014. **35**(9): p. 8483-8523.
3. Rothman, K. and A. Keller, *The effect of joint exposure to alcohol and tobacco on risk of cancer of the mouth and pharynx.* Journal of chronic diseases, 1972. **25**(12): p. 711-716.
4. Carbone, D., *Smoking and cancer.* The American Journal of Medicine, 1992. **93**(1, Supplement 1): p. S13-S17.
5. Siegel, R.L., K.D. Miller, and A. Jemal, *Cancer statistics, 2016.* CA: a cancer journal for clinicians, 2016. **66**(1): p. 7-30.
6. Ryerson, A.B., et al., *Annual Report to the Nation on the Status of Cancer, 1975-2012, featuring the increasing incidence of liver cancer.* Cancer, 2016. **122**(9): p. 1312-1337.
7. Statistics, N.C.f.H., *Health, United States, 2016: With Chartbook on Long-term Trends in Health.* Hyattsville, Maryland.
8. Ferlay, J., et al., *Cancer incidence and mortality worldwide: Sources, methods and major patterns in GLOBOCAN 2012.* International Journal of Cancer, 2015. **136**(5): p. E359-E386.
9. *Cancer*. February 2018 [cited 2017 February 12]; Available from: http://www.who.int/mediacentre/factsheets/fs297/en/.

10. Vairaktaris, E., et al., *The hamster model of sequential oral oncogenesis.* Oral Oncology, 2008. **44**(4): p. 315-324.

11. Howlader, N., et al., *SEER Cancer Statistics Review, 1975–2014, National Cancer Institute. Bethesda.* 2015.

12. Merletti, F., et al., *Role of Tobacco and Alcoholic Beverages in the Etiology of Cancer of the Oral Cavity/Oropharynx in Torino, Italy.* Cancer Research, 1989. **49**(17): p. 4919.

13. Block, G., B. Patterson, and A. Subar, *Fruit, vegetables, and cancer prevention: a review of the epidemiological evidence.* Nutrition and cancer, 1992. **18**(1): p. 1-29.

14. Petersen, P.E., *Oral cancer prevention and control – The approach of the World Health Organization.* Oral Oncology, 2009. **45**(4–5): p. 454-460.

15. Warnakulasuriya, S., *Global epidemiology of oral and oropharyngeal cancer.* Oral Oncology, 2009. **45**(4–5): p. 309-316.

16. Lingen, M.W., et al., *Critical Evaluation of Diagnostic Aids for the Detection of Oral Cancer.* Oral oncology, 2008. **44**(1): p. 10-22.

17. Wilson, J.M.G. and G. Jungner, *Principles and practice of screening for disease.* Principles and practice of screening for disease., 1968(34).

18. Hinsdale, T., et al., *Optically sectioned wide-field fluorescence lifetime imaging microscopy enabled by structured illumination.* Biomedical Optics Express, 2017. **8**(3): p. 1455-1465.

19. Costas, B., *Review of biomedical optical imaging—a powerful, non-invasive, non-ionizing technology for improving in vivo diagnosis.* Measurement Science and Technology, 2009. **20**(10): p. 104020.

20. Abercrombie, M., *Estimation of nuclear population from microtome sections.* The Anatomical Record, 1946. **94**(2): p. 239-247.

21. Cheng, S., et al., *Handheld multispectral fluorescence lifetime imaging system for in vivo applications.* Biomedical Optics Express, 2014. **5**(3): p. 921-931.

22. Cheng, S., et al., *Flexible endoscope for continuous in vivo multispectral fluorescence lifetime imaging.* Optics Letters, 2013. **38**(9): p. 1515-1517.

23. Jabbour, J.M., et al., *Fluorescence lifetime imaging and reflectance confocal microscopy for multiscale imaging of oral precancer.* Journal of Biomedical Optics, 2013. **18**(4): p. 046012-046012.

24. Lane, P.M., et al., *Simple device for the direct visualization of oral-cavity tissue fluorescence.* Journal of Biomedical Optics, 2006. **11**(2): p. 024006-024006-7.

25. Takano, J.H., et al., *Detecting early oral cancer: narrowband imaging system observation of the oral mucosa microvasculature.* International Journal of Oral and Maxillofacial Surgery, 2010. **39**(3): p. 208-213.

26. Griffiths, D. and E. Harris, *Introduction to Quantum Mechanics.* American journal of physics, 1995. **63**(8): p. 767-768.

27. Milonni, P.W., *Why spontaneous emission?* American Journal of Physics, 1984. **52**(4): p. 340-343.

28. Yokoyama, H. and K. Ujihara, *Spontaneous emission and laser oscillation in microcavities*. Vol. 10. 1995: CRC press.

29. Scully, M., M.S. Zubairy, and I. Walmsley, *Quantum Optics.* American journal of physics, 1999. **67**(7): p. 648-648.

30. Fox, M., *Quantum optics: an introduction*. Vol. 15. 2006: OUP Oxford.

31. Solé, J.G., L.E. Bausá, and D. Jaque, *Appendix A3: The Calculation of the Probability of Spontaneous Emission by Means of Einstein's Thermodynamic Treatment*, in *An Introduction to the Optical Spectroscopy of Inorganic Solids*. 2005, John Wiley & Sons, Ltd. p. 271-273.

32. Grewe, B.F., et al., *Fast two-layer two-photon imaging of neuronal cell populations using an electrically tunable lens.* Biomedical Optics Express, 2011. **2**(7): p. 2035-2046.

33. van Munster, E.B. and T.W.J. Gadella, *Fluorescence Lifetime Imaging Microscopy (FLIM)*, in *Microscopy Techniques: -/-*, J. Rietdorf, Editor. 2005, Springer Berlin Heidelberg: Berlin, Heidelberg. p. 143-175.

34. Berezin, M.Y. and S. Achilefu, *Fluorescence Lifetime Measurements and Biological Imaging.* Chemical Reviews, 2010. **110**(5): p. 2641-2684.

35. Lattarulo, C., et al., *Microscopic Imaging of Intracellular Calcium in Live Cells Using Lifetime-Based Ratiometric Measurements of Oregon Green BAPTA-1*, in *Neurodegeneration: Methods and Protocols*, G. Manfredi and H. Kawamata, Editors. 2011, Humana Press: Totowa, NJ. p. 377-389.

36. Lakowicz, J.R., et al., *Fluorescence lifetime imaging of free and protein-bound NADH.* Proceedings of the National Academy of Sciences, 1992. **89**(4): p. 1271-1275.

37. Skala, M.C., et al., *In vivo Multiphoton Fluorescence Lifetime Imaging of Protein-bound and Free NADH in Normal and Pre-cancerous Epithelia.* Journal of biomedical optics, 2007. **12**(2): p. 024014-024014.

38. Skala, M.C., et al., *In vivo multiphoton microscopy of NADH and FAD redox states, fluorescence lifetimes, and cellular morphology in precancerous epithelia.* Proceedings of the National Academy of Sciences, 2007. **104**(49): p. 19494-19499.

39. Zheng, J.I.E., *Energy metabolism of cancer: Glycolysis versus oxidative phosphorylation (Review).* Oncology Letters, 2012. **4**(6): p. 1151-1157.

40. Maeda-Yorita, K. and K. Aki, *Effect of Nicotinamide Adenine Dinucleotide on the Oxidation-Reduction Potentials of Lipoamide Dehydrogenase from Pig Heart.* The Journal of Biochemistry, 1984. **96**(3): p. 683-690.

41. Santala, M., et al., *Type I and type III collagen metabolites as predictors of clinical outcome in epithelial ovarian cancer.* Clinical cancer research, 1999. **5**(12): p. 4091-4096.

42. Wahl, M., *TIme-Correlated Single Photon Couning.* PicoQuant, 2014.

43. Moore, C., et al., *Comparison of Methods for Rapid Evaluation of Lifetimes of Exponential Decays.* Applied Spectroscopy, 2004. **58**(5): p. 603-607.

44. Saxena, M., G. Eluru, and S.S. Gorthi, *Structured illumination microscopy.* Advances in Optics and Photonics, 2015. **7**(2): p. 241-275.

45. Neil, M.A.A., R. Juškaitis, and T. Wilson, *Method of obtaining optical sectioning by using structured light in a conventional microscope.* Optics Letters, 1997. **22**(24): p. 1905-1907.

46. Chasles, F., B. Dubertret, and A.C. Boccara, *Optimization and characterization of a structured illumination microscope.* Optics Express, 2007. **15**(24): p. 16130-16140.

47. Poher, V., et al., *Optical sectioning microscopes with no moving parts using a micro-stripe array light emitting diode.* Optics Express, 2007. **15**(18): p. 11196-11206.

48. Schaefer, L.H., D. Schuster, and J. Schaffer, *Structured illumination microscopy: artefact analysis and reduction utilizing a parameter optimization approach.* Journal of Microscopy, 2004. **216**(2): p. 165-174.

49. Neil, M.A.A., R. Juškaitis, and T. Wilson, *Real time 3D fluorescence microscopy by two beam interference illumination.* Optics Communications, 1998. **153**(1–3): p. 1-4.

50. Dan, D., et al., *DMD-based LED-illumination Super-resolution and optical sectioning microscopy.* Scientific Reports, 2013. **3**: p. 1116.

51. Förster, R., et al., *Simple structured illumination microscope setup with high acquisition speed by using a spatial light modulator.* Optics Express, 2014. **22**(17): p. 20663-20677.

52. Wilson, T., *Confocal Microscopy*. 1990: Acad. Press.

53. Wilson, T. and C. Sheppard, *Theory and practice of scanning optical microscopy*. Vol. 180. 1984: Academic Press London.

54. Wilson, T. and A.R. Carlini, *Size of the detector in confocal imaging systems.* Optics Letters, 1987. **12**(4): p. 227-229.

55. Wilson, T., *Resolution and optical sectioning in the confocal microscope.* Journal of Microscopy, 2011. **244**(2): p. 113-121.

56. Karadaglić, D. and T. Wilson, *Image formation in structured illumination wide-field fluorescence microscopy.* Micron, 2008. **39**(7): p. 808-818.

57. Jabbour, J.M., et al., *Confocal Endomicroscopy: Instrumentation and Medical Applications.* Annals of Biomedical Engineering, 2012. **40**(2): p. 378-397.

58. Chen, L., et al., *Remote focal scanning optical projection tomography with an electrically tunable lens.* Biomedical Optics Express, 2014. **5**(10): p. 3367-3375.

59. Fahrbach, F.O., et al., *Rapid 3D light-sheet microscopy with a tunable lens.* Optics Express, 2013. **21**(18): p. 21010-21026.

60. Jabbour, J.M., et al., *Optical axial scanning in confocal microscopy using an electrically tunable lens.* Biomedical Optics Express, 2014. **5**(2): p. 645-652.

61. Koukourakis, N., et al., *Axial scanning in confocal microscopy employing adaptive lenses (CAL).* Optics Express, 2014. **22**(5): p. 6025-6039.

62. Riza, N.A., et al., *Demonstration of three-dimensional optical imaging using a confocal microscope based on a liquid-crystal electronic lens.* Optical Engineering, 2008. **47**(6): p. 063201-063201-9.

63. Jabbour, J.M., et al., *Reflectance confocal endomicroscope with optical axial scanning for in vivo imaging of the oral mucosa.* Biomedical Optics Express, 2014. **5**(11): p. 3781-3791.

64. Fuchs, F.S., et al., *Confocal laser endomicroscopy for diagnosing lung cancer in vivo.* European Respiratory Journal, 2013. **41**(6): p. 1401-1408.

65. Neumann, H., et al., *Confocal laser endomicroscopy: technical advances and clinical applications.* Gastroenterology, 2010. **139**(2): p. 388-392. e2.

66. Polglase, A.L., et al., *A fluorescence confocal endomicroscope for in vivo microscopy of the upper-and the lower-GI tract.* Gastrointestinal endoscopy, 2005. **62**(5): p. 686-695.

67. Ozbay, B.N., et al., *Miniaturized fiber-coupled confocal fluorescence microscope with an electrowetting variable focus lens using no moving parts.* Optics letters, 2015. **40**(11): p. 2553-2556.

68. York, A.G., et al., *Resolution doubling in live, multicellular organisms via multifocal structured illumination microscopy.* Nature methods, 2012. **9**(7): p. 749-754.

69. Gulledge, C. and M. Dewhirst, *Tumor oxygenation: a matter of supply and demand.* Anticancer research, 1995. **16**(2): p. 741-749.

70. Squire, A. and P.I.H. Bastiaens, *Three dimensional image restoration in fluorescence lifetime imaging microscopy.* Journal of Microscopy, 1999. **193**(1): p. 36-49.

71. Sharman, K.K., et al., *Error Analysis of the Rapid Lifetime Determination Method for Double-Exponential Decays and New Windowing Schemes.* Analytical Chemistry, 1999. **71**(5): p. 947-952.

72. Cole, M.J., et al., *Time-domain whole-field fluorescence lifetime imaging with optical sectioning.* Journal of Microscopy, 2001. **203**(3): p. 246-257.

73. Hagen, N., L. Gao, and T.S. Tkaczyk, *Quantitative sectioning and noise analysis for structured illumination microscopy.* Optics Express, 2012. **20**(1): p. 403-413.

74. Banerjee, S. and D. Bhatt, *Histochemical studies on the distribution of certain dehydrogenases in squamous cell carcinoma of cheek.* Indian journal of cancer, 1989. **26**(1): p. 21-30.

75. Thomas, P., et al., *Biochemical Imaging of Human Atherosclerotic Plaques with Fluorescence Lifetime Angioscopy.* Photochemistry and Photobiology, 2010. **86**(3): p. 727-731.

76. Kristoffersen, A.S., et al., *Testing Fluorescence Lifetime Standards using Two-Photon Excitation and Time-Domain Instrumentation: Rhodamine B, Coumarin 6 and Lucifer Yellow.* Journal of Fluorescence, 2014. **24**(4): p. 1015-1024.

77. Smith, S.W., *The Scientist and Engineer's Guide to Digital Signal Processing*. 1997: California Technical Pub.

78. Coda, S., et al., *Fluorescence lifetime spectroscopy of tissue autofluorescence in normal and diseased colon measured ex vivo using a fiber-optic probe.* Biomedical Optics Express, 2014. **5**(2): p. 515-538.

79. Zheng, W., et al., *Autofluorescence of epithelial tissue: single-photon versus two-photon excitation.* Journal of biomedical optics, 2008. **13**(5): p. 054010-054010-8.

80. Pavlova, I., et al., *Understanding the Biological Basis of Autofluorescence Imaging for Oral Cancer Detection: High-Resolution Fluorescence Microscopy in Viable Tissue.* Clinical Cancer Research, 2008. **14**(8): p. 2396-2404.

81. Wu, Y. and J.Y. Qu, *Combined depth- and time-resolved autofluorescence spectroscopy of epithelial tissue.* Optics Letters, 2006. **31**(12): p. 1833-1835.

82. Wang, M., et al., *Rapid diagnosis and intraoperative margin assessment of human lung cancer with fluorescence lifetime imaging microscopy.* BBA Clinical, 2017. **8**: p. 7-13.

83. Malik, B.H., et al., *Objective detection of oral carcinoma with multispectral fluorescence lifetime imaging in vivo.* Photochemistry and Photobiology, 2016. **92**(5): p. 694-701.

84. Zhao, Q., I.T. Young, and J.G.S.d. Jong. *Photon budget analysis for fluorescence lifetime imaging microscopy*. 2011. SPIE.

85. Fu, H.L., et al., *Optimization of a Widefield Structured Illumination Microscope for Non-Destructive Assessment and Quantification of Nuclear Features in Tumor Margins of a Primary Mouse Model of Sarcoma.* PLOS ONE, 2013. **8**(7): p. e68868.

86. Wilcox, R.R., *New Designs in Analysis of Variance.* Annual Review of Psychology, 1987. **38**(1): p. 29-60.

87. Mital C. Shingala, D.A.R., *Comparison of Post Hoc Tests for Unequal Variance.* International Journal of New Technologies in Science and Engineering, 2015. **2**(5).

88. Pan, X. and C.E. Metz, *The "Proper" binormal model: Parametric receiver operating characteristic curve estimation with degenerate data.* Academic Radiology, 1997. **4**(5): p. 380-389.

89. Fukatsu, K., et al., *Microscopic Invasion Patterns and Epithelial Cell-phenotypes in Early Gastric Cancer with Submucosal Invasion.* Journal of Cytology & Histology, 2015. **6**(6): p. 1.

90. Hoffman, Z.R. and C.A. DiMarzio. *Single-image structured illumination using Hilbert transform demodulation*. 2017. SPIE.

91. Olsovsky, C., et al. *Handheld tunable focus confocal microscope utilizing a double-clad fiber coupler for <italic>in vivo</italic> imaging of oral epithelium*. 2017. SPIE.

92. Zhu, W., N. Zeng, and N. Wang, *Sensitivity, specificity, accuracy, associated confidence interval and ROC analysis with practical SAS implementations.* NESUG proceedings: health care and life sciences, Baltimore, Maryland, 2010. **19**: p. 67.

93. Riley, R.D., et al., *Summarising and validating test accuracy results across multiple studies for use in clinical practice.* Statistics in medicine, 2015. **34**(13): p. 2081-2103.

94. Leeflang, M.M., et al., *Systematic reviews of diagnostic test accuracy.* Annals of internal medicine, 2008. **149**(12): p. 889-897.

95. Thuiller, W., et al., *Vulnerability of African mammals to anthropogenic climate change under conservative land transformation assumptions.* Global Change Biology, 2006. **12**(3): p. 424-440.

96. Thuiller, W., et al., *Niche-based modelling as a tool for predicting the risk of alien plant invasions at a global scale.* Global Change Biology, 2005. **11**(12): p. 2234-2250.